UNIVERSITY OF CALIFORNIA SAN DIEGO

An Integrated Mechanochemical Model of Sperm Locomotion

A Thesis submitted in partial satisfaction of the requirements
for the degree Master of Science

in

Engineering Sciences (Mechanical Engineering)

by

Chenji Li

Committee in charge:

Professor David Saintillan, Chair
Professor Padmini Rangamani
Professor Oliver Schmidt

2021

The Thesis of Chenji Li is approved, and it is acceptable in quality and form for publication on microfilm and electronically.

University of California San Diego

2021

TABLE OF CONTENTS

LIST OF FIGURES

LIST OF TABLES

ACKNOWLEDGEMENTS

The two years at UCSD have been a fantastic journey for me, especially the research work I've done under the guidance of my advisor David Saintillan. Before I found the balance between absorption and output, David has always been patient with me. He not only provided me with all the resources but also gave me sufficient space and courage to start thinking of my own. Through but not limited to every Zoom meeting in the pandemic, David guided me to dig deep into the detail of each equation while also take control of the overall direction. When it comes to the choice of future development, David freely shared with me his professional experience and gave me as much help as possible for me to take the forward step to my next career stage. Thank you for all the guidance and inspiration!

I would like to thank my senior Brato Chakrabarti for unreservedly offering support and improvement through my whole learning and coding process. I am also thankful to Achal Mahajan and Mohammadhossein Firouznia for all the caring and suggestions on both academic and daily life.

There has never been a word in my vocabulary to explain my love and gratitude to my family. The pandemic paused the traffic of the world, but it didn't cut off the communication of love. Thank you for offering unconditional encouragement and faith, so that I can keep trying to be the person I have always dream to be.

I dedicate this last paragraph to my fiancee. Before we getting too old to recall our whole life, I have to write a long memoir to record all of the great journeys we have experienced together. By that time, I will quote this paragraph after the chapter from the bustling city of Beijing to the sunny beaches of San Diego, to start the next chapter of our life in the peaceful and beautiful midwest town.

ABSTRACT OF THE THESIS

An Integrated Mechanochemical Model of Sperm Locomotion

by

Chenji Li

Master of Science in Engineering Sciences (Mechanical Engineering)

University of California San Diego, 2021

Professor David Saintillan, Chair

Mammalian sperm cells manage locomotion by the movement of their flagella. Dynein motors inside the flagellum consume energy from ATP to exert active sliding forces between microtubule doublets, thus creating bending waves along the flagellum and enabling the sperm cell to swim in a viscous medium. Recently, a model has been proposed for the planar nonlinear beating of the flagellum under clamped and hinged boundary conditions, where spontaneous oscillations emerged from the coupling of dynein motor kinetics with deformations. In a new framework combining slender-body theory and the boundary element method, we extend this model to study the free swimming of sperm cells with arbitrary head shapes, considering the effects of non-local hydrodynamic interactions between head and flagellum. The model is shown

to produce realistic beating patterns and swimming trajectories, which we analyze as a function of sperm number and motor activity. Remarkably, we find that the swimming velocity does not vary monotonically with motor activity, but instead displays two local maxima corresponding to distinct modes of swimming.

Chapter 1

Introduction

The spermatozoon, or sperm cell is the male gamete reproductive cell that contains the genetic information. The tail of the sperm cell is known as flagellum, normally possessing motility that enables the delivery of the genetic material to the egg. The sexual fertilization process of mammals makes it extremely hard for the sperm cell to reach the egg, where only successful sperm, part of a population of hundreds of millions, can survive through this process [1]. Because sperm cells are allogenic to the female, they may encounter the defenses of the female immune system meant for infectious organisms [4]. To maintain the fertility, sperm cells have to take advantage of their resources like motility to survive from the selection and elimination [5], while such a selection process often takes place in highly viscous non-Newtonian liquids.

Studying sperm cell motility has significant meaning to the mammalian fertility. About one fifth of couples are infertile, and half of them are caused by the male partner due to abnormal semen quality [6, 7]. The advent of in vitro fertilization (IVF) has greatly helped couples who are unable to have children. On the other hand, developing a safely reversible nonhormonal male contraception method could assist preventing the unwanted pregnancy [8]. Motility of sperm has been observed to have a strong relation to the fertility [9, 10]. Sperm swimming velocity, it turns out, is particularly important to its competitive advantage of fertilization [11, 12, 13, 14, 15, 16].

Other swimming characteristics like head trajectory, beating frequency and amplitude have also been observed to have correlation with fertility [10, 17].

Mammalian sperm cell has a head that packs the genetic information, connected with a flagellum beating actively and pushing the cell swimming forward. As illustrated by Figure 1.1, the axoneme is the inner core of the flagellum that generates the bending for the motility of the sperm cell. The cross section of the flagellum has nine microtubule pairs centered around a pair of singlet microtubules, known as the '9+2' structure [18]. Active dynein motors provide flagellum activity with the energy coming from ATP hydrolysis. A group of dynein motors, attached to one of the microtubules and walking along the other one, exert sliding forces between the microtubules [19].

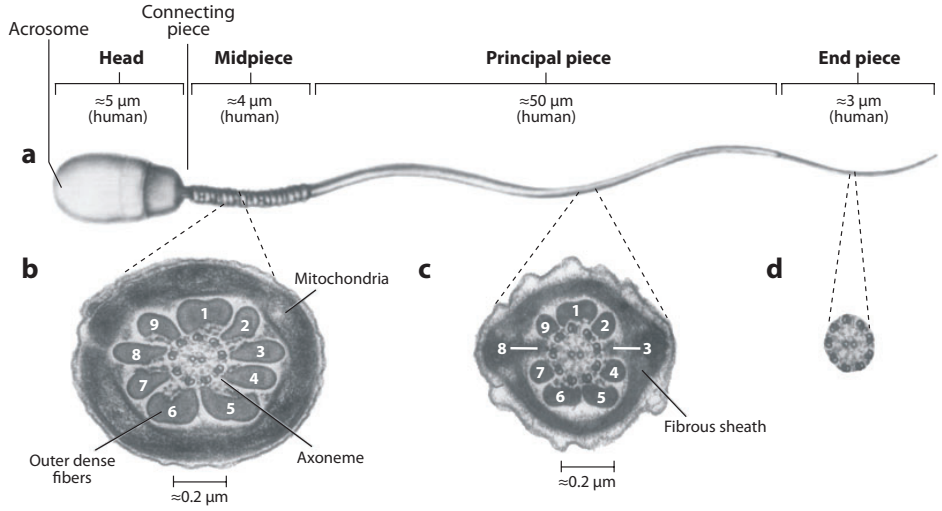

Figure 1.1: Microscopic observation of Spermatozoa Structure (Reproduced from [1, 2, 3])

The typical value of the Reynolds number for a sperm cell has the order of 10^{-3}, so that the viscous force plays a much more important role in the system than the inertial force. Under the environment of low Reynolds number flow, hydrodynamics analysis first gives to resistive force theory, which offers a linear relation between the hydrodynamic viscous force and velocity in the tangential and normal directions, respectively [20, 21]. Associated with resistive force theory,

slender body theory also provides a relation between force and velocity around slender-body, with hydrodynamic interactions being considered to satisfy the no-slip boundary condition on the body [22, 23, 24].

While the flagellum has been usually modeled as an Euler-Bernoulli filament, a lot of efforts have been made to explain the active movement of sperm cell. It has been proposed that the steady dynein forces can produce propulsive oscillations [25, 26]. More realistic to biological mechanism, geometric feedback control models include the on and off activity of molecular motors [27, 28, 29, 30].

A sliding control model recently has been proposed by Oriola *et al.* [31], which coupled the dynein kinetics to the shape of flagellum. Chakrabarti *et al.* [32] further complete the model by considering the interaction, and gives numerically solvable governing equations. The results showed the existence of a second transition where the direction of wave propagation reversed for a clamped flagellum. In this thesis, I further improved the model of Chakrabarti *et al.* [32] and studied the motility of sperm cell with coupled interaction between head and flagellum being considered. I find the existence of a second transition in the similar form of Chakrabarti's work [32], but marked by a change in the characteristic of the head trajectory and beating mode, with the wave propagation direction going from base to tip.

Chapter 2

Sperm Cell Model

In this chapter, we show the process of building a detailed bottom-up model for the sperm locomotion. In the model, we use a sliding control model to simulate the geometric feedback on the force exerted by active dynein motors, which drives the flagellum's spontaneous beating in the viscous medium. Within the regime of low Reynolds number, slender body theory and boundary integral method are used here to include the long-range hydrodynamic interaction into the system.

2.1 Geometric and Kinetic Description

2.1.1 Shape of Sperm Cell

The shape of the sperm head can vary from one mammalian to the other [33, 34]. To keep the universality of this model, we kept the shape of the head to be an arbitrary 3D shape in the whole modeling process. In the simulation results,we will use an ellipsoidal shape. The flagellum in the model has a cylindrical shape connected with the head, and the connection is assumed to be clamped.

It has been observed that the sperm cell beating is mostly planar. We describe the flagellum deformation and kinetics in 2D where most of it can be captured. Note that 2D frame here is

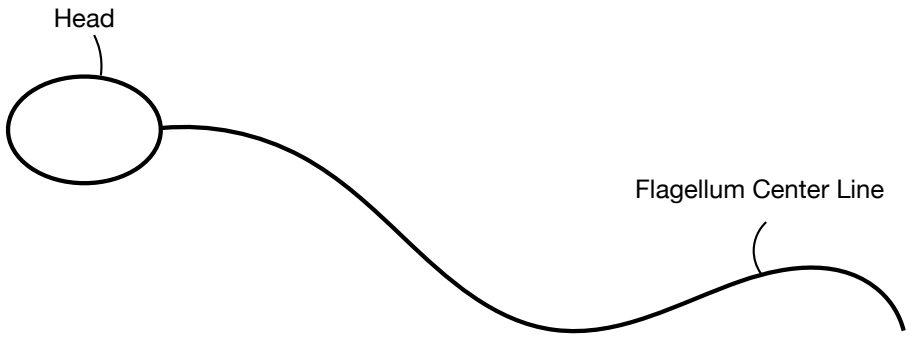

Figure 2.1: Geometry description of sperm cell

only used for deformation, both head and flagellum still have 3D geometric shapes, and the hydrodynamic interactions also act in the 3D domain. As shown in Figure 2.1, we use the center line of the flagellum to define its shape.

2.1.2 Frame of Reference

In both experiment and simulation, the lab frame of reference is the most common and most directly method to describe the geometry information. However, in the process of modeling, numerical, and post processing, other frames of reference can also be very useful and convenient. Here we describe four observation systems that will be used.

Lab frame of reference: For the lab frame, $\hat{\mathbf{e}}_x$ and $\hat{\mathbf{e}}_x$ are two unit vectors in Cartesian coordinates.

Flagellum local coordinate system: For slender structure like flagellum, it is very convenient to define variables along the flagellum, especially when the flagellum in this problem is assumed to be inextensible, and the hydrodynamic resistance perform differently on tangential and normal direction. As shown in Figure 2.2, s is the arc length along the flagellum, while $s = 0$ and $s = L$ represent the base end and the tip end of flagellum. At each point on the flagellum, $\hat{\mathbf{t}}$ and $\hat{\mathbf{n}}$ are unit vectors on local tangential and normal direction, and $\phi(s,t)$ is the angle between $\hat{\mathbf{t}}$ and $\hat{\mathbf{e}}_x$.

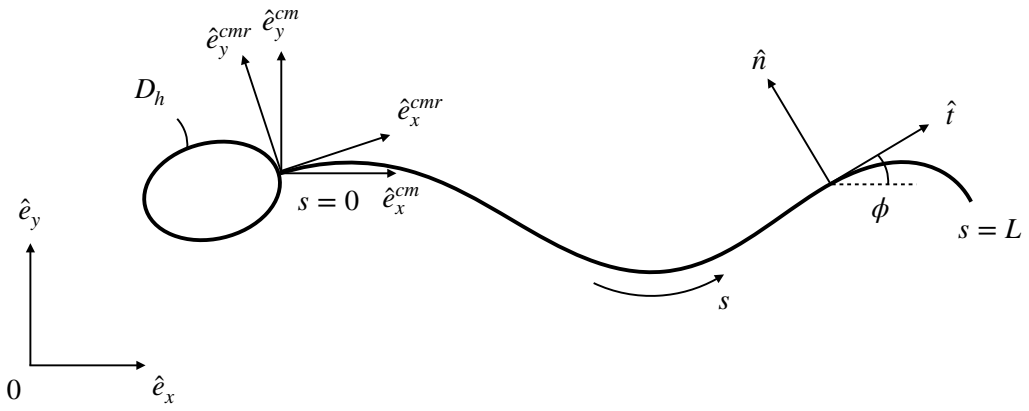

Figure 2.2: Four frame of reference for geometric description

Co-moving frame: The origin point of the co-moving frame is fixed at the joint point between head and flagellum, while staying parallel with the lab frame. Two base unit vectors are $\hat{\mathbf{e}}_x^{cm}$ and $\hat{\mathbf{e}}_y^{cm}$. Within the co-moving frame we can have the sperm cell fixed in the frame to observe the beating and rotation clearer. Also, it can be used to analyze the data in flow field during the swimming.

Co-moving-rotating frame: By rotating the co-moving frame to keep $\hat{\mathbf{e}}_x^{cmr}$ and $\hat{\mathbf{e}}_y^{cmr}$ aligned with $\hat{\mathbf{t}}(s=0,t)$ and $\hat{\mathbf{n}}(s=0,t)$ respectively, we get the co-moving-rotating frame. Note that no head movement will be observed under this frame, which can speed up the numerical solver for the head. We will discuss this in more detail in Chapter 3.

To increase the readability, here we list some useful relations. The translation between lab frame and the local perspective is

$$\hat{\mathbf{t}} = \hat{\mathbf{e}}_x cos\phi + \hat{\mathbf{e}}_y sin\phi \tag{2.1}$$

$$\hat{\mathbf{n}} = -\hat{\mathbf{e}}_x sin\phi + \hat{\mathbf{e}}_y cos\phi \tag{2.2}$$

We define the derivative of $\phi(s,t)$ with respect to the arc length as the curvature, written

as $\kappa = \partial_s \phi$. Since $\hat{\mathbf{e}}_x$ and $\hat{\mathbf{e}}_y$ are constants, by taking space and time derivatives of $\hat{\mathbf{t}}$ and $\hat{\mathbf{n}}$, we get

$$\partial_s \hat{\mathbf{t}} = \kappa \hat{\mathbf{n}} \tag{2.3}$$

$$\partial_s \hat{\mathbf{n}} = -\kappa \hat{\mathbf{t}} \tag{2.4}$$

$$\partial_t \hat{\mathbf{t}} = \dot{\phi} \hat{\mathbf{n}} \tag{2.5}$$

$$\partial_t \hat{\mathbf{n}} = -\dot{\phi} \hat{\mathbf{t}} \tag{2.6}$$

For the translation between co-moving frame and co-moving-rotating frame, here we introduce the rotation matrix $\mathbf{R}$, so that $\mathbf{x}^{cmr} = \mathbf{R}\mathbf{x}^{cm}$.

2.1.3 Kinetics of Sperm Cell

When the position of the head is known, the function $\phi(s,t)$ itself can fully describe the geometric and kinetic information of the sperm cell:

$$\mathbf{x}_f(s) = \mathbf{x}_f(0) + \int_0^s \hat{\mathbf{t}}(s')ds' \tag{2.7}$$

where $\mathbf{x}_f(s)$ is the position of flagellum in lab frame, and the flagellum velocity is

$$\mathbf{v}(s) = \mathbf{v}(0) + \int_0^s \dot{\phi}(s')\hat{\mathbf{n}}(s')ds' \tag{2.8}$$

D_h shown in Figure 2.2 is the surface of the head. As in Figure 2.3 (a), we first use $\mathbf{x}_h^{cmr}(s)$ define the geometric shape of the head by its surface in co-moving-rotating frame, where $\mathbf{x}_h^{cmr}(s)$ is a known constant for non-deformable head. Since the head is clamped with the flagellum, we can have kinetic information of each point on the head with $\phi(0)$ and $\mathbf{x}_f(0)$, as in Figure 2.3 (b):

$$\mathbf{x}_h = \mathbf{x}_f(0) + \mathbf{R}'\mathbf{x}_h^{cmr} \tag{2.9}$$

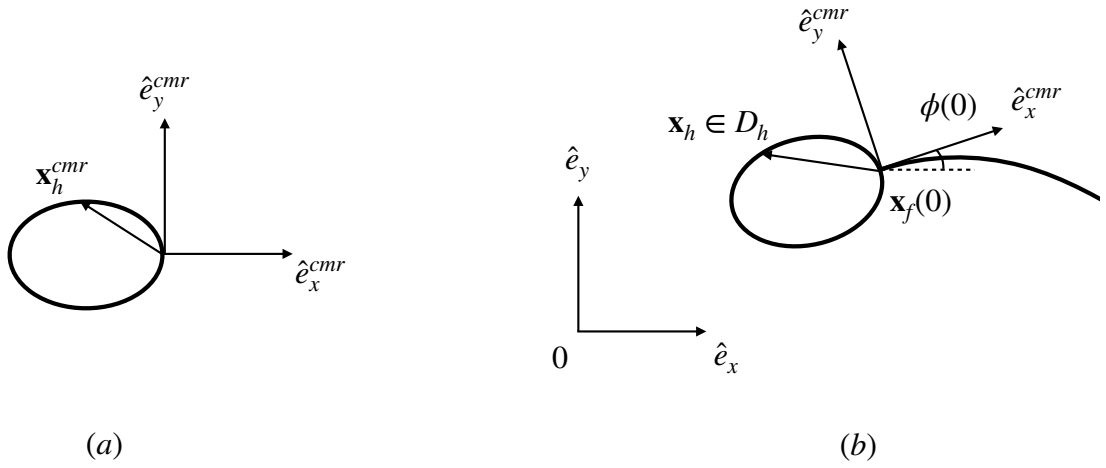

Figure 2.3: (a) Geometric shape of head in co-moving-rotating frame. (b) Geometric shape of head in lab frame.

where $\mathbf{R}'$ is the inverse of $\mathbf{R}$, defined the transition from co-moving-rotating frame to co-moving frame.

For the velocity of flagellum $\mathbf{v}(s) = v_T\hat{\mathbf{t}} + v_N\hat{\mathbf{n}}$, here is an important relation that we will need for later use. With the relation given above, the spatial derivative of velocity along the arc length is

$$\partial_s\mathbf{v} = (\partial_s v_T - \phi_s v_N)\hat{\mathbf{t}} + (\partial_s v_N + \phi_s v_T)\hat{\mathbf{n}} \tag{2.10}$$

On the other hand, $\partial_s\mathbf{v} = \partial_s\partial_t\mathbf{x} = \partial_t\partial_s\mathbf{x}$. Since we know that $\partial_s\mathbf{x} = \hat{\mathbf{t}}$, we also have

$$\partial_s\mathbf{v} = \phi_t\hat{\mathbf{n}} \tag{2.11}$$

For Equation (2.10) and (2.11) to be both satisfied, we find

$$\partial_s v_T = \phi_s v_N \tag{2.12}$$

$$\partial_s v_N = \phi_t - \phi_s v_T \tag{2.13}$$

2.2 Dynamics of Locomotion

The beating of sperm can be proved to have low Reynolds number, meaning that inertia is negligible compared to viscosity of the system. In the absence of the inertia, the system stays balanced for each time instant. In this section, we derive the force and moment balance equations, and give the corresponding scalar expressions for planar beating.

2.2.1 Force and Moment in System

Flagellum can be regarded as a passive elastic rod when the sperm cell is inactive. The internal force along the flagellum is $\mathbf{F} = T\hat{\mathbf{t}} + N\hat{\mathbf{n}}$, where T and N are tangent and normal components of the internal force. For an elastic rod, the internal moment along the flagellum is $\mathbf{M} = B\partial_s\phi\hat{\mathbf{k}}$, with B the bending rigidity of the flagellum. The force density distribution on the flagellum is defined as $\mathbf{f}_f = \frac{\partial \mathbf{F}}{\partial s}$. Based on Equations (2.3) and (2.4), we have

$$\mathbf{f}_f = (T_s - N\phi_s)\hat{\mathbf{t}} + (N_s + T\phi_s)\hat{\mathbf{n}} \tag{2.14}$$

The viscous force density acting on the flagellum is written as $\mathbf{f}_{vis} = q_T\hat{\mathbf{t}} + q_N\hat{\mathbf{n}}$. Here q_T and q_N components of viscous force on $\hat{\mathbf{t}}$ and $\hat{\mathbf{n}}$ direction.

The force density distribution on the head is defined as $\mathbf{f}_h$ for $\mathbf{x}_h \in D_h$.

It will be proved in the later section that the activity of dynein motors only shows up as an active moment acting on flagellum, which we will denote as $\mathbf{n}$

2.2.2 Balance Equations of flagellum

For a segment from s_1 to s_2, the internal force at two sides should balanced with the total viscous force on the flagellum, written as

$$\int_{s_1}^{s_2} \mathbf{f}_{vis} ds + \mathbf{F}(s)\Big|_{s_1}^{s_2} = 0 \tag{2.15}$$

This balance equation has to be satisfied for an arbitrary segment, which gives

$$\mathbf{f}_{vis} + \frac{\partial \mathbf{F}}{\partial s} = 0 \tag{2.16}$$

This can also be written as

$$\mathbf{f}_f = -\mathbf{f}_{vis} \tag{2.17}$$

Similarly for the moment balance, we can first write down the balance equation for s_1 to s_2 segment

$$\int_{s_1}^{s_2} (\mathbf{n}(s) + \mathbf{x}(s) \times \mathbf{f}_{vis})\, ds + (\mathbf{M}(s) + \mathbf{x}(s) \times \mathbf{F}(s)) \Big|_{s_1}^{s_2} = 0 \tag{2.18}$$

With Equation (2.16), the equation at arclength s becomes

$$\mathbf{n}(s) + \frac{\partial \mathbf{M}}{\partial s} + \partial_s \mathbf{x} \times \mathbf{F} = 0 \tag{2.19}$$

2.2.3 Scalar Expression in Planar Beating

Equations (2.16) and (2.19) are the balance equations for the flagellum. By projecting these two equations onto $\hat{\mathbf{t}}$, $\hat{\mathbf{n}}$, and $\hat{\mathbf{k}}$ directions, we get the scalar expressions of the balance equation for the planar beating of the flagellum:

$$T_s - N\phi_s + q_T = 0 \tag{2.20}$$

$$N_s + T\phi_s + q_N = 0 \tag{2.21}$$

$$M_s + n + N = 0 \tag{2.22}$$

2.3 Activity

Instead of seeing the flagellum as a passive elastic rod with superimposed beating, here we model the flagellum as an active filament. The spontaneous bending of the flagellum exerted by the dynein motors is modeled in this section, with the sliding control model providing the density coefficients and sliding force. The geometric deformation and hydrodynamic perturbation created by the swimming motion of the cell will be the factor that defines the activity, and thus gives rise to spontaneous oscillations.

2.3.1 Micro Structure and its 2D Projection

With the fact that the beating of flagellum is mostly planar, here we simplify the 3D structure by projecting it onto the 2D plane. As illustrated in Figure 2.4, the axoneme has been simplified as two filaments, with dynein motors and nexin links working between them.

2.3.2 Bending and Sliding Displacement

With the sliding force exerted by the dynein motors, two filaments tend to slide relative to each other. Since both filaments are connected to the head where no displacement can happen, sliding displacement for flagellum shows up as bending in the end. As marked in Figure 2.4, $\mathbf{x}$ is the position of the flagellum center line. $\hat{\mathbf{t}}$ and $\hat{\mathbf{n}}$ are unit vectors on tangential and normal direction, and a is the diameter of the flagellum. We use $\mathbf{x}_+$ and $\mathbf{x}_-$ to describe the shape of two filaments, where we have

$$\mathbf{x}_+ = \mathbf{x} + \frac{a}{2}\hat{\mathbf{n}} \tag{2.23}$$

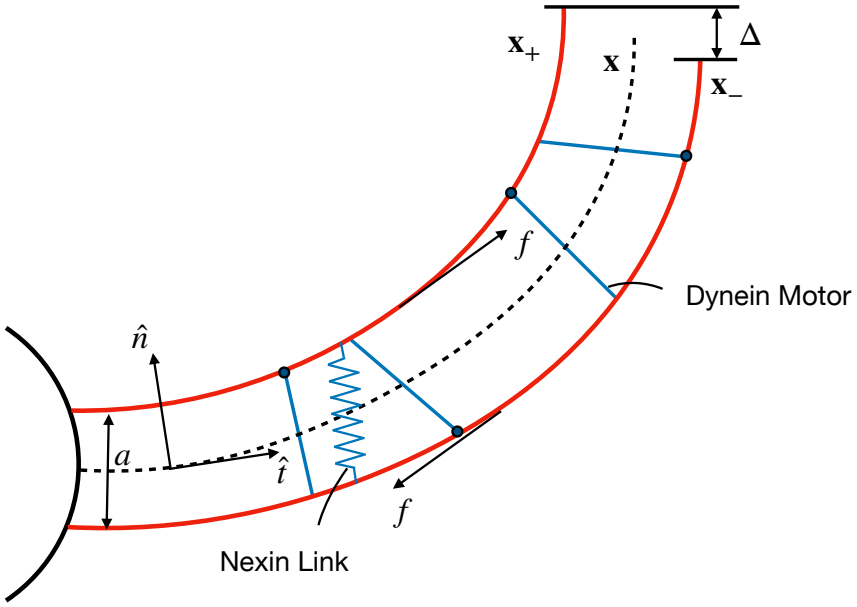

Figure 2.4: Two-dimensional simplification for planar beating

$$\mathbf{x}_- = \mathbf{x} - \frac{a}{2}\hat{\mathbf{n}} \tag{2.24}$$

Δ is the sliding displacement between the filaments, this can be calculated by the arc length difference for a specific location.

$$\Delta = \int_0^s \left[\left| \partial_s \mathbf{x}_-(s') \right| - \left| \partial_s \mathbf{x}_+(s') \right| \right] ds' \tag{2.25}$$

Note that we have the relation $\partial_s \hat{\mathbf{n}} = -\kappa \hat{\mathbf{t}}$, and therefore

$$\Delta = a \int_0^s \kappa ds' \tag{2.26}$$

Since curvature is defined as $\kappa = \partial_s \phi$, we find the relation between sliding displacement and local angle as

$$\Delta = a\left[\phi(s) - \phi(0)\right] \tag{2.27}$$

2.3.3 Sliding Force

The sliding force between filaments is decided by both dynein activity and nexin resistance. As shown in Figure 2.4, dynein motors attached to one filament are 'walking' along the other filament. This 'walking' process is a combination of repeated binding and unbinding.

Following Oriola *et al.* [31], here we model the sliding force density as

$$f(s,t) = \rho(n_+F_+ + n_-F_-) - K\Delta \tag{2.28}$$

In this equation, $f(s,t)$ is the sliding force acting on unit length of filament given by dynein motor and nexin links. $\rho = \mathcal{N}/L$ defines the average density of dynein motors along filaments, when $\mathcal{N}$ is the total number of the dynein motors and L is the total length of flagellum. n_+ and n_- are density coefficients that define the fractions of dynein motors in the bound state. F_+ and F_- are the local sliding force exerted by a single bound motor. K is the spring stiffness of nexin links, while Δ is the local sliding displacement.

By the Newton's third law of motion, sliding force acting on these two filament has equal magnitude and opposite direction. This means there will be no active force in macroscopic view acting on the flagellum. Instead, it shows up as an active moment n. Centered around the flagellum center line, the active moment is given as

$$n(s) = \frac{a}{2}\hat{\mathbf{n}} \times (-f\hat{\mathbf{t}}) + (-\frac{a}{2}\hat{\mathbf{n}}) \times f\hat{\mathbf{t}} = af\hat{\mathbf{k}} \tag{2.29}$$

where $\hat{\mathbf{k}}$ is the unit vector pointing out of the plane.

2.3.4 Motor Kinetics

To fully describe the sliding force given by dynein motors, we also need to provide a model for binding and unbinding process. The total number of dynein motor along the flagellum

$\mathscr{N}$ is a constant. As defined before, n_+ and n_- are fractions of bounded dynein motors, which is the part of dynein motors that are exerting the sliding force. We express the bind rate for a single dynein motor as $\pi_\pm$, and unbind rate as $\varepsilon_\pm$, so that the rate of change of $n_\pm$ can be written as

$$\partial_t n_\pm = \pi_\pm - \varepsilon_\pm \tag{2.30}$$

The binding rate of dynein motor is proportional to the local fraction of unbound motors, thus

$$\pi_\pm = \pi_0(1 - n_\pm) \tag{2.31}$$

where π_0 is a constant, indicating a characteristic binding rate.

The unbinding rate is proportional to the local fraction of bound motors, and also exponentially decided by the loading

$$\varepsilon_\pm = \varepsilon_0 n_\pm exp(F_\pm / f_c) \tag{2.32}$$

in which ε_0, similarly, is a characteristic unbinding rate. f_c is the critical load that defines the transition when the unbinding will start to happen massively.

The force exerted by a single bound dynein motor is assumed to have a linear relations with the local sliding velocity

$$F_\pm = \pm f_0(1 \mp \Delta_t / v_0) \tag{2.33}$$

where f_0 is the stall force when there is no dynein motion. $\Delta_t(s) = a(\phi_t(s) - \phi_t(0))$ is the sliding velocity, and v_0 is the zero load velocity.

By combining Equations (2.30), (2.31), (2.32) and (2.33), we get the governing equation for the rate of change of the density coefficients:

$$\partial_t n_\pm = \pi_0(1 - n_\pm) - \varepsilon_0 n_\pm exp[\frac{f_0}{f_c}(1 \mp \Delta_t / v_0)] \tag{2.34}$$

By combining Equations (2.33) and (2.28), the sliding force equation becomes

$$f(s,t) = f_0\rho(\bar{n} - \frac{\Delta_t}{v_0}\tilde{n}) - K\Delta \tag{2.35}$$

where $\bar{n} = n_+ - n_-$, $\tilde{n} = n_+ + n_-$.

2.4 Hydrodynamic Interaction

The sperm cell experiences viscous drag as it swims through the medium. In this section, we show that the inertia is negligible given the low Reynolds number of the system. The viscous force density acting on the flagellum is expressed by the slender body theory, while the hydrodynamics of the head is captured by the boundary integral method.

2.4.1 Low Reynolds Number and Stokeslet

The ratio of inertial force and viscous force in fluid system can be expressed by its Reynolds number, defined as

$$Re = \frac{\rho UL}{\mu} \tag{2.36}$$

The scales of the flow environment for the current biology system we are exploring shows to have very small Reynolds number ($\mathcal{O}(10^{-5} - 10^{-4})$). This indicates the flow to be creeping flow, with negligible inertial force.

When $Re \to 0$, the Navier-Stokes equations simplify as the Stokes equations

$$-\mu\nabla^2\mathbf{u} + \nabla p = \rho\mathbf{b} \tag{2.37}$$

$$\nabla \cdot \mathbf{u} = 0 \tag{2.38}$$

When the force in the system is distributed as a delta function

$$-\mu\nabla^2\mathbf{u}+\nabla p=\mathbf{g}\delta(\mathbf{x}-\mathbf{x}_0), \tag{2.39}$$

we know the solution for Stokes equation can be written as

$$u_i(x)=\frac{1}{8\pi\mu}G_{ij}(\mathbf{x},\mathbf{x}_0)g_j \tag{2.40}$$

where G_{ij} is the Green's function.

For our problem with sperm cell swimming in the free-space, we have the Green's function as Stokeslet

$$G_{ij}(\hat{\mathbf{x}})=\frac{\delta_{ij}}{r}+\frac{\hat{x}_i\hat{x}_j}{r^3} \tag{2.41}$$

where $r=|\hat{\mathbf{x}}|$, $\hat{\mathbf{x}}=\mathbf{x}-\mathbf{x}_0$.

2.4.2 Slender Body Theory

The viscous force acting on flagellum is captured by the slender body theory, considering the flagellum-self interaction and head-to-flagellum interaction. The velocity of the flagellum is decided by the force distribution on both head and flagellum, written as

$$8\pi\nu\mathbf{v}=\mathscr{M}[\mathbf{f}_f]+\mathscr{H}[\mathbf{f}_h] \tag{2.42}$$

Here the operator $\mathscr{M}$ has two contributions $\mathscr{M}=\mathscr{L}+\mathscr{K}$. The local part $\mathscr{L}[\mathbf{f}_f]$ gives the viscous force by the local velocity within the quiescent environment.

$$\mathscr{L}[\mathbf{f}_f](s)=[\frac{1}{\xi_\perp}\hat{\mathbf{n}}(s)\hat{\mathbf{n}}(s)+\frac{1}{\xi_\parallel}\hat{\mathbf{t}}(s)\hat{\mathbf{t}}(s)]\cdot\mathbf{f}_\mathbf{f}(s) \tag{2.43}$$

Two friction coefficients in the local operator, $\xi_\perp$ and $\xi_\parallel$ indicate that the resistance force

on slender body has different performance on tangential and normal direction, defined as

$$\xi_{\parallel} = -\frac{1}{2c}, \quad \xi_{\perp} = \frac{1}{2-c} \tag{2.44}$$

where $c = log(\varepsilon^2 e) < 0$ with $\varepsilon = a/L$.

$\mathscr{K}[\mathbf{f}_f]$ and $\mathscr{H}[\mathbf{f}_h]$ capture the viscous force due to the hydrodynamic interactions, in which $\mathscr{K}[\mathbf{f}_f]$ is the contribution for non-local flagellum perturbation.

$$\mathscr{K}[\mathbf{f}_f](s) = \int_0^L \left[\frac{\mathbf{I} + \hat{\mathbf{R}}(s,s')\hat{\mathbf{R}}(s,s')}{|\mathbf{R}(s,s')|} \cdot \mathbf{f}_{\mathbf{f}}(s') - \frac{\mathbf{I} + \hat{\mathbf{t}}(s)\hat{\mathbf{t}}(s)}{|s-s'|} \cdot \mathbf{f}_{\mathbf{f}}(s) \right] ds' \tag{2.45}$$

where $\mathbf{R}(s,s') = \mathbf{x}_f(s) - \mathbf{x}_f(s')$ and $\hat{\mathbf{R}} = \mathbf{R}/|\mathbf{R}|$.

$\mathscr{H}[\mathbf{f}_h]$ is the hydrodynamic interaction contributed by the head

$$\mathscr{H}[\mathbf{f}_h] = \iint_{D_h} \mathbf{G}(\mathbf{x}_f(s), \mathbf{x}'_h) \cdot \mathbf{f}_h(\mathbf{x}'_h) dD'_h \tag{2.46}$$

in which $\mathbf{G}$ is the Stokeslet, which gives

$$\mathscr{H}[\mathbf{f}_h] = \iint_{D_h} \left(\frac{\mathbf{I}}{|\mathbf{r}(\mathbf{x}_f, \mathbf{x}'_h)|} + \frac{\mathbf{r}(\mathbf{x}_f, \mathbf{x}'_h)\mathbf{r}(\mathbf{x}_f, \mathbf{x}'_h)}{|\mathbf{r}(\mathbf{x}_f, \mathbf{x}'_h)|^3} \right) \cdot \mathbf{f}_h(\mathbf{x}'_h) dD'_h \tag{2.47}$$

where $\mathbf{r}(\mathbf{x}_f, \mathbf{x}'_h) = \mathbf{x}_f(s) - \mathbf{x}'_h$.

2.5 Governing Equations

In the previous section, we have finished modeling the dynamic system centered around the force and moment balance equation. The active and viscous terms are given by the sliding control model and slender body theory. In this section, we combine the models and present the comprehensive governing equations.

For the nonlocal terms $\mathscr{K}[\mathbf{f}_f]$ and $\mathscr{H}[\mathbf{f}_h]$ in slender body theory, we group their projection

of tangential and normal direction as

$$u_t^d(s) = \left(\mathscr{K}[\mathbf{f}_f](s) + \mathscr{H}[\mathbf{f}_h](s)\right) \cdot \hat{\mathbf{t}}(s) \tag{2.48}$$

$$u_n^d(s) = \left(\mathscr{K}[\mathbf{f}_f](s) + \mathscr{H}[\mathbf{f}_h](s)\right) \cdot \hat{\mathbf{n}}(s) \tag{2.49}$$

We can now project the slender body theory onto $\hat{\mathbf{t}}$ and $\hat{\mathbf{n}}$

$$8\pi\nu v_T = \frac{1}{\xi_\parallel}\hat{\mathbf{t}} \cdot \mathbf{f_f} + u_t^d \tag{2.50}$$

$$8\pi\nu v_N = \frac{1}{\xi_\perp}\hat{\mathbf{n}} \cdot \mathbf{f_f} + u_n^d \tag{2.51}$$

With the fact that $\mathbf{f}_f = -\mathbf{f}_{vis}$ and $\mathbf{f}_{vis} = q_T\hat{\mathbf{t}} + q_N\hat{\mathbf{n}}$, the viscous force in the force balance equation can be expressed by

$$q_T = (u_t^d - 8\pi\nu v_T)\xi_\parallel \tag{2.52}$$

$$q_N = (u_n^d - 8\pi\nu v_N)\xi_\perp \tag{2.53}$$

The scalar force balance equations (2.20) and (2.21) then become

$$T_s - N\phi_s + (u_t^d - 8\pi\nu v_T)\xi_\parallel = 0 \tag{2.54}$$

$$N_s + T\phi_s + (u_n^d - 8\pi\nu v_N)\xi_\perp = 0 \tag{2.55}$$

To eliminate the velocity terms v_T and v_N in the system, we use the velocity relation that has been proved above. After plugging Equations (2.54) and (2.55) into (2.12) and (2.11), we get the force and balance equation on tangential and normal direction as

$$T_{ss} - N\phi_{ss} - (1 + \frac{\xi_\parallel}{\xi_\perp})N_s\phi_s - \frac{\xi_\parallel}{\xi_\perp}T\phi_s^2 = \xi_\parallel(\phi_s u_n^d - \partial_s u_t^d) \tag{2.56}$$

$$N_{ss} + T\phi_{ss} + (1 + \frac{\xi_\perp}{\xi_\parallel})T_s\phi_s - \frac{\xi_\perp}{\xi_\parallel}N\phi_s^2 = \xi_\perp(8\pi\nu\phi_t - u_t^d\phi_s - \partial_s u_n^d) \tag{2.57}$$

For a flagellum regarded as elastic beam, the bending torque is given as $M = EI\phi_s$. We substitute Equation (2.29) into (2.22), so that we get the moment balance equation as

$$EI\phi_{ss} + af + N = 0 \tag{2.58}$$

We now have had a closed system of governing equations, namely Equations (2.56), (2.57), (2.58), (2.35), (2.34).

2.6 Boundary Conditions

The boundary condition at the base end of flagellum is given by the force and moment balance equations on the head. The head of the sperm cell itself has no motility and is pushed, dragged and rotated by the force and torque coming from the flagellum through the clamping connection. As inertia is negligible, we write down the force and moment balance equation for the head as

$$\mathbf{F}(0) - \iint_{D_h} \mathbf{f}_h(x_h')dD_h' = 0 \tag{2.59}$$

$$\mathbf{x}_f(0) \times \mathbf{F}(0) + \mathbf{M}(0) - \iint_{D_h} x_h' \times \mathbf{f}_h(x_h')dD_h' = 0 \tag{2.60}$$

The distal end of the flagellum has force free and moment free conditions, which are

$$\mathbf{F}(L) = 0 \tag{2.61}$$

$$\mathbf{M}(L) = 0 \tag{2.62}$$

With the definition of bending torque, $\mathbf{M}(L) = 0$ can also be written as $\phi_s(L) = 0$. As for the expression of $\mathbf{M}(0)$, we need to start with Equation (2.18) by setting s_1 to 0 and s_2 to L. With

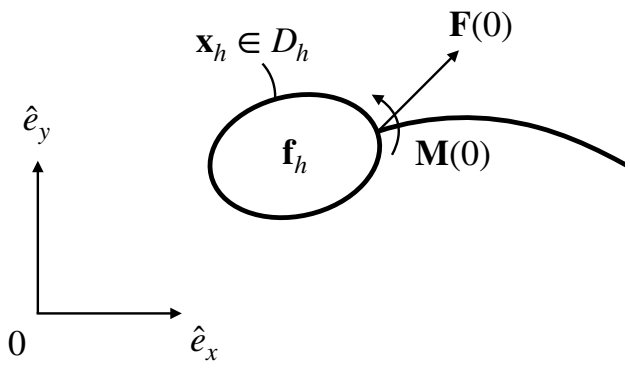

Figure 2.5: Force and moment acting on the head.

the moment free boundary condition at the distal end, the bending torque at the base end is given as $\mathbf{M}(0) = \int_0^L N ds$. We rewrite equation (2.5) as

$$\mathbf{x}(0) \times \mathbf{F}(0) + \int_0^L N ds - \iint_{D_h} x'_h \times \mathbf{f}_h(x'_h) dD'_h = 0 \tag{2.63}$$

On both the flagellum and head surface, we have the no-slip boundary condition. The one for the flagellum has been given by slender body theory. To capture the no-slip condition on the head surface, we first write down the velocity of the head surface as the rigid body motion

$$\mathbf{v}_h = \mathbf{v}(0) + \dot{\phi}(0)\hat{\mathbf{k}} \times \bar{\mathbf{x}} \tag{2.64}$$

The velocity of the fluid flow at the same place on the head surface is given by the boundary integral method as

$$\mathbf{v}'_h = \frac{1}{8\pi\nu} \left[\int_0^L \mathbf{G}(\mathbf{x}_h, \mathbf{x}'_f) \mathbf{f}_f(\mathbf{x}'_f) dS'_f + \iint_{D_h} \mathbf{G}(\mathbf{x}_h, \mathbf{x}'_h) \mathbf{f}_h(\mathbf{x}'_h) dD'_h \right] \tag{2.65}$$

where the first term on the right hand side corresponds to the flow created by the flagellum beating, and the second term correspond to the flow perturbed by head.

The no-slip boundary condition requires the velocity of the rigid body to be the same as the velocity of the fluid at the same place, which gives

$$\begin{aligned}\int_0^L \mathbf{G}(\mathbf{x}_h,\mathbf{x}'_f)\mathbf{f}_f(\mathbf{x}'_f)dS'_f + \iint_{D_h} \mathbf{G}(\mathbf{x}_h,\mathbf{x}'_h)\mathbf{f}_h(\mathbf{x}'_h)dD'_h \\ = 8\pi\nu\left(\mathbf{v}(0)+\dot{\phi}(0)\hat{\mathbf{k}}\times\bar{\mathbf{x}}\right)\end{aligned} \tag{2.66}$$

2.7 Nondimensionalization

We now nondimensionalize the system with characteritic scales for the system. The macroscopical length is nondimensionalized by the are-length L of sperm cell, while the microscopic length scale is the diameter a of flagellum. Scale for time is chosen to be the characteristic time $\tau_0 = 1/(\varepsilon_0+\pi_0)$. The density of the sliding force between the filaments is scaled by ρf_0, and the elastic force in the flagellum is scaled by B/L^2.

By applying nondimensionalization to the corresponding variables in the system, we obtain several important dimensionless parameters:

- $Sp = L(8\pi\nu\xi_\perp/B\tau_0)^{1/4}$
- $\mu_a = a\rho f_0 L^2/B$
- $\mu = Ka^2L^2/B$
- $\zeta = a/(v_0\tau_0)$

Sp is the sperm number, represent the bending rigidity of the system by comparing the time scale of bending relaxation to motor correlation time. Note that larger sperm number indicates less rigid flagellum. μ_a measures the active force compared to the bending force and indicates the activity of the flagellum. Larger μ_a gives more active sperm cell. μ is the ratio between resistance from the nexin links and the bending, reporting the stiffness of the system. ζ compares the diameter of flagellum to the characteristic displacement due to motor activity. Also,

we define $\eta = \pi_0/(\varepsilon_0 + \pi_0)$, and $\bar{f} = f_0/f_c$. Then the governing equations become

$$T_{ss} - N\phi_{ss} - (1 + \frac{\xi_\parallel}{\xi_\perp})N_s\phi_s - \frac{\xi_\parallel}{\xi_\perp}T\phi_s^2 = \xi_\parallel(\phi_s u_n^d - \partial_s u_t^d) \tag{2.67}$$

$$N_{ss} + T\phi_{ss} + (1 + \frac{\xi_\perp}{\xi_\parallel})T_s\phi_s - \frac{\xi_\perp}{\xi_\parallel}N\phi_s^2 = Sp^4\phi_t - \xi_\perp(u_t^d\phi_s + \partial_s u_n^d) \tag{2.68}$$

$$\phi_{ss} + \mu_a f + N = 0 \tag{2.69}$$

$$f = \bar{n} - \zeta\tilde{n}\Delta_t - \frac{\mu}{\mu_a}\Delta \tag{2.70}$$

$$\partial_t n_\pm = \eta(1 - n_\pm) - (1 - \eta)n_\pm exp[\bar{f}(1 \mp \zeta\Delta_t)] \tag{2.71}$$

in which all the variables are dimensionless.

Similarly for boundary conditions, we have

$$\mathbf{F}(0) = \iint_{D_h} \mathbf{f}_h(x_h')dD_h' \tag{2.72}$$

$$\mathbf{x}(0) \times \mathbf{F}(0) + \int_0^1 Nds = \iint_{D_h} x_h' \times \mathbf{f}_h(x_h')dD_h' \tag{2.73}$$

$$\mathbf{F}(1) = 0 \tag{2.74}$$

$$\mathbf{M}(1) = 0 \tag{2.75}$$

$$\begin{aligned} &\int_0^L \mathbf{G}(\mathbf{x}_h, \mathbf{x}_f')\mathbf{f}_f(\mathbf{x}_f')dS_f' + \iint_{D_h} \mathbf{G}(\mathbf{x}_h, \mathbf{x}_h')\mathbf{f}_h(\mathbf{x}_h')dD_h' \\ &= \frac{Sp^4}{\xi_\perp}\left(\mathbf{v}(0) + \dot{\phi}(0)\hat{\mathbf{k}} \times \bar{\mathbf{x}}\right) \end{aligned} \tag{2.76}$$

$$\frac{Sp^4}{\xi_\perp}\mathbf{v} = \mathscr{L}[\mathbf{f}_f] + \mathscr{K}[\mathbf{f}_f] + \mathscr{H}[\mathbf{f}_h] \tag{2.77}$$

Chapter 3

Numerical Methods

Previously, we presented the nondimensionalized governing equations and boundary conditions for the sperm model. In this chapter, we present the numerical method for solving the nonlinear system. By separating the system into equations for the head and flagellum dynamics, we can use both explicit and implicit methods to march in time. The advantage of each method is discussed, and detailed process of both solver is explained.

3.1 Separated System

The two components of the sperm cell, head and flagellum, are clamped with each other. The geometric description of the head and flagellum is done differently during the modeling process. For the flagellum, we use its center line to describe the shape, while for the head we use the surface. Even though in the system both of them are 3D objects with a surface to be evaluated, here we have to handle them separately because of their different geometric description.

We now name the equations we have into two groups, namely, the equations for the head and flagellum, so that we can discuss their solver separately.

All five governing equations in the system are applied to the flagellum. Under the assumption of negligible inertial, the system is balanced at any time instant. Ideally, we would

like to solve the system at a given time instant as fast and accurately as possible. To make the flagellum solvable at a time, we start with two balance equations (2.67) and (2.68). Recall that $\Delta = \phi - \phi(0)$, $\Delta_t = \phi_t - \phi_t(0)$, here we have a time derivative term ϕ_t on the right hand side of equations (2.68), which can be eliminated by combining them with Equation (2.69) and (2.70):

$$\begin{aligned} &\mu_a \zeta \tilde{n} \left[N_{ss} + T\phi_{ss} + (1 + \frac{\xi_\perp}{\xi_\parallel}) T_s \phi_s - \frac{\xi_\perp}{\xi_\parallel} N \phi_s^2 \right] - Sp^4 N = \\ &Sp^4 \left[\phi_{ss} + \mu_a \bar{n} + \mu_a \zeta \tilde{n} \dot{\phi}(0) - \mu \left(\phi - \phi(0) \right) \right] - \xi_\perp \mu_a \zeta \tilde{n} \left(u_t^d \phi_s + \partial_s u_n^d \right) \end{aligned} \tag{3.1}$$

$$T_{ss} - N\phi_{ss} - (1 + \frac{\xi_\parallel}{\xi_\perp}) N_s \phi_s - \frac{\xi_\parallel}{\xi_\perp} T \phi_s^2 = \xi_\parallel (\phi_s u_n^d - \partial_s u_t^d) \tag{3.2}$$

Equation (2.74) and (2.75) are nominated as the boundary conditions for the distal end of the flagellum, and Equation (2.77) at the connecting point will be used as the boundary condition for the base end of the flagellum.

As for the head, we have Equation (2.76) as the governing equations, while Equations (2.72) and (2.73) work as the boundary conditions.

3.2 Explicit and Implicit

For the two parts of equation for flagellum and head, neither of the part is closed. More specifically, for the equation of flagellum we have $\dot{\phi}(0)$ in the governing equation, and $\mathbf{v}(0)$ in the boundary condition. These are the velocity and angular velocity of head, which should be given by the head part of the system. Similarly in the head part of the system, there are $\mathbf{F}(0)$, $\int_0^1 N ds$, $\mathbf{f}_f$, which are all the variables for the flagellum that has to be given by the solution of flagellum part.

These features of the system indicates that the two parts for flagellum and head are a coupled system. The first option would be solving them explicitly, which means each part of system is solved directly with all the necessary input information. Say we start the simulation

with an initial guess based on the information from previous time steps, for example the velocity and angular velocity of flagellum. Then we solve the part of flagellum by itself and use its results to solve for the part of head, then doing it iteratively. Note that during this process, each step of the solving process has all the necessary values and can be solved efficiently, which is the advantage of using explicit method. One disadvantage is that we need to run multiple iterations for each time step to reach its convergence. Also the system can be relatively unstable when using the explicit method, so that the system can keep running stably only with very small time step size. To reach to the same total time length, more steps of calculation have to be processed.

The other option is to use the implicit scheme to solve the system. We notice that only terms that the flagellum part needs are the head velocity and angular velocity. If we can manage to express the head velocity and angular velocity explicitly in terms of the information from the flagellum itself, we no longer need the iteration and can solve the system for a time instant by one step calculation. The numerical scheme becomes more stable with the implicit scheme, which gives us the chance to use hundreds of times larger time step size to reach to same time length with much fewer steps. This feature gives us the chance to better search in the parameter plane.

Note that the implicit method generally is not guaranteed to be faster than the explicit method, because each step consumes more work to be done. In this paper, we proposed both explicit and implicit schemes. Numerical simulations show that the implicit scheme can be faster with larger time step size, while each step takes around 10 times longer than the explicit method.

3.3 Discretization and Finite Difference

To translate the equation numerically, we discretize the flagellum along its arc length, with a total number of N_f nodes evenly distributed on the flagellum. $h = 1/(N_f - 1)$ is the size of grid on flagellum. Head surface is discretized as a mesh with a total number of N_h triangles.

3.3.1 Solver for Flagellum

Equation (3.1) and (3.2) are the two equations we want to solve numerically here. Assuming the shape and non-local interaction terms are unknown, these two equations now become linear in the two unknowns N and T. The derivative terms are given by finite differences with second order accuracy. For the grid point with index j on the flagellum ($j \neq 1, j \neq N_f$), the equations can be written as

$$\begin{aligned}
&\mu_a \zeta \tilde{n} \left[\frac{N^{j-1} - 2N^j + N^{j+1}}{h^2} + \phi_{ss} T^j + \left(1 + \frac{\xi_\perp}{\xi_\parallel}\right) \phi_s \frac{T^{j+1} - T^{j-1}}{2h} - \frac{\xi_\perp}{\xi_\parallel} \phi_s^2 N^j \right] \\
&- Sp^4 N^j = Sp^4 \left[\phi_{ss} + \mu_a \bar{n} + \mu_a \zeta \tilde{n} \dot{\phi}(0) - \mu \left(\phi - \phi(0) \right) \right] \\
&- \xi_\perp \mu_a \zeta \tilde{n} \left(u_t^d \phi_s + \partial_s u_n^d \right)
\end{aligned} \tag{3.3}$$

$$\begin{aligned}
&\frac{T^{j-1} - 2T^j + T^{j+1}}{h^2} - \phi_{ss} N^j - \left(1 + \frac{\xi_\parallel}{\xi_\perp}\right) \phi_s \frac{N^{j+1} - N^{j-1}}{2h} \\
&- \frac{\xi_\parallel}{\xi_\perp} \phi_s^2 T^j = \xi_\parallel (\phi_s u_n^d - \partial_s u_t^d)
\end{aligned} \tag{3.4}$$

We introduce the notation $k = \mu_a \zeta \tilde{n}$. The right hand sides of both equations are known, and now written as b_1 and b_2. We can thus further simplify the equation as

$$\begin{aligned}
&\frac{k}{h^2} N^{j-1} + \left(-\frac{2k}{h^2} - \frac{\xi_\perp}{\xi_\parallel} k \phi_s^2 - Sp^4 \right) N^j + \frac{k}{h^2} N^{j+1} \\
&+ \left[-\left(1 + \frac{\xi_\perp}{\xi_\parallel}\right) \frac{k}{2h} \phi_s \right] T^{j-1} + k \phi_{ss} T^j + \left[\left(1 + \frac{\xi_\perp}{\xi_\parallel}\right) \frac{k}{2h} \phi_s \right] T^{j+1} = b_1^j
\end{aligned} \tag{3.5}$$

$$\begin{aligned}
&\left[\left(1 + \frac{\xi_\parallel}{\xi_\perp}\right) \frac{1}{2h} \phi_s \right] N^{j-1} + (-\phi_{ss}) N^j + \left[-\left(1 + \frac{\xi_\parallel}{\xi_\perp}\right) \frac{1}{2h} \phi_s \right] N^{j+1} \\
&+ \frac{1}{h^2} T^{j-1} + \left(-\frac{2}{h^2} - \frac{\xi_\parallel}{\xi_\perp} \phi_s^2 \right) T^j + \frac{1}{h^2} T^{j+1} = b_2^j
\end{aligned} \tag{3.6}$$

The numerical system then can be written as

$$\mathbf{A}_{NT} \cdot \overrightarrow{\mathbf{F}}_{NT} = \mathbf{b} \tag{3.7}$$

in which $\overrightarrow{\mathbf{F}}_{NT} = [N^1, T^1, N^2, T^2, N^3, T^3, ...]$ is the merge vector of N and T. Similarly, $\mathbf{b}$ is the merge vector of b_1 and b_2. $\mathbf{A}_{NT}$ is a $2N_f \times 2N_f$ matrix including the coefficients given by Equation (3.5) and (3.6).

The first two and last two rows of $\mathbf{A}_{NT}$ should be defined separately based on the boundary conditions. The force free boundary condition at the distal end shows up in the last two rows as

$$N^{N_f} = 0 \tag{3.8}$$

$$T^{N_f} = 0 \tag{3.9}$$

The boundary condition at the base end is given by the slender body theory when $s = 0$:

$$\frac{Sp^4}{\xi_\perp} v_T(0) = \frac{1}{\xi_\parallel}(T_s - N\phi_s) + u_t^d \tag{3.10}$$

$$\frac{Sp^4}{\xi_\perp} v_N(0) = \frac{1}{\xi_\perp}(N_s + T\phi_s) + u_n^d \tag{3.11}$$

In the form of finite difference, the first two rows of $\mathbf{A}_{NT}$ read

$$(-\phi_s)N^1 + \left(-\frac{3}{2h}\right)T^1 + \frac{2}{h}T^2 + \left(-\frac{1}{2h}\right)T^3 = Sp^4 \frac{\xi_\parallel}{\xi_\perp} v_T(0) - \xi_\parallel u_t^d(0) \tag{3.12}$$

$$\left(-\frac{3}{2h}\right)N^1 + \frac{2}{h}N^2 + \left(-\frac{1}{2h}\right)N^3 + \phi_s T^1 = Sp^4 v_N(0) - \xi_\perp u_n^d(0) \tag{3.13}$$

With Equation (3.5), (3.6), (3.8), (3.9), (3.12), (3.13), $\mathbf{A}_{NT}$ and $\mathbf{b}$ has been fully defined. Thus we can solve the flagellum part and get the force distribution along the flagellum.

3.3.2 Solver for Head

Assume that we know the shape of the flagellum and $\mathbf{F}(s)$, which can be used to calculate $\mathbf{f}_f$. And $\mathbf{v}(0)$, $\dot{\phi}(0)$, $\mathbf{f}_h$ are the unknowns we need to solve here. We start with Equation (2.76), and choose the center point of the element with index j, we have

$$\begin{aligned}\int_0^L \mathbf{G}(\mathbf{x}_h^j, \mathbf{x}_f')\mathbf{f}_f(\mathbf{x}_f')dS_f' + \iint_{D_h} \mathbf{G}(\mathbf{x}_h^j, \mathbf{x}_h')\mathbf{f}_h(\mathbf{x}_h')dD_h' \\ = \frac{Sp^4}{\xi_\perp}\left(\mathbf{v}(0) + \dot{\phi}(0)\hat{\mathbf{k}} \times \bar{\mathbf{x}}\right)\end{aligned} \tag{3.14}$$

Note that integral here is already the numerical operator. With known flagellum shape and non-deformable head clamped with flagellum, the Green's function $\mathbf{G}(\mathbf{x}_h^j, \mathbf{x}_f')$ and $\mathbf{G}(\mathbf{x}_h^j, \mathbf{x}_h')$ that govern the interactions are known here. This equation has to be satisfied for each element on the head, so that the system can be written as

$$\mathbf{A}_{hh} \cdot \overrightarrow{\mathbf{f}_h} + \mathbf{A}_{hf} \cdot \overrightarrow{\mathbf{f}_f} = \frac{Sp^4}{\xi_\perp}\left(\overrightarrow{\mathbf{v}(0)} + \dot{\phi}(0)\overrightarrow{\hat{\mathbf{k}} \times \bar{\mathbf{x}}}\right) \tag{3.15}$$

where $\mathbf{A}_{hh}$ includes the information of surface integral and Green's function for two elements on flagellum, and $\mathbf{A}_{hf}$ includes the line integral and interaction between the element on the head and the grid on flagellum. $\overrightarrow{\mathbf{f}_h}$ and $\overrightarrow{\mathbf{f}_f}$ are the matrix containing all the force distribution for head and flagellum. Similar for $\overrightarrow{\mathbf{v}(0)}$ and $\overrightarrow{\hat{\mathbf{k}} \times \bar{\mathbf{x}}}$.

Then the force distribution on the head reads as

$$\overrightarrow{\mathbf{f}_h} = -\mathbf{A}_{hh}^{-1} \cdot \mathbf{A}_{hf} \cdot \overrightarrow{\mathbf{f}_f} + \frac{Sp^4}{\xi_\perp}\mathbf{A}_{hh}^{-1} \cdot \left(\overrightarrow{\mathbf{v}(0)} + \dot{\phi}(0)\overrightarrow{\hat{\mathbf{k}} \times \bar{\mathbf{x}}}\right) \tag{3.16}$$

The first term on the right hand side is known, while the second one isn't as it involve the unknown velocity and angular velocity of the head. These quantities will be given by the force and moment balance equation on the head. To finish this step, first we need to define the force response of the unit movement when the head is swimming by itself in the quiescent flow.

Table 3.1: Force response of unit movement for head swimming in quiescent flow.

Unit Movement	Force distribution	Total force and moment
$v_T(0)=1$ $v_N(0)=0$ $\dot{\phi}(0)=0$	$\mathbf{f}_T^q(\mathbf{x}_h)$	$\mathbf{F}_T^q = \iint_{D_h} \mathbf{f}_T^q(\mathbf{x}'_h) dD'_h$
$v_T(0)=0$ $v_N(0)=1$ $\dot{\phi}(0)=0$	$\mathbf{f}_N^q(\mathbf{x}_h)$	$\mathbf{F}_N^q = \iint_{D_h} \mathbf{f}_N^q(\mathbf{x}'_h) dD'_h$
$v_T(0)=0$ $v_N(0)=0$ $\dot{\phi}(0)=1$	$\mathbf{f}_K^q(\mathbf{x}_h)$	$\mathbf{F}_K^q = \iint_{D_h} \mathbf{f}_K^q(\mathbf{x}'_h) dD'_h$ $\mathbf{M}_K^q = \iint_{D_h} \mathbf{x}'_h \times \mathbf{f}_K^q(\mathbf{x}'_h) dD'_h$

For non-deformable head, $\mathbf{f}_T^q$, $\mathbf{f}_N^q$, $\mathbf{f}_K^q$, $\mathbf{F}_T^q$, $\mathbf{F}_N^q$, $\mathbf{F}_K^q$ and $\mathbf{M}_K^q$ are all constants in the co-moving-rotating frame. Recall that Stokes flow is linear, meaning the force in the system has a linear relation with the velocity. Based on Table 3.1, force distribution for the head swimming in the quiescent flow is

$$\mathbf{f}_h^q = v_T(0)\mathbf{f}_T^q + v_N(0)\mathbf{f}_N^q + \dot{\phi}(0)\mathbf{f}_K^q(\mathbf{x}_h) \tag{3.17}$$

Now go back to Equation (3.16), the second term on the right hand side is the force due to the self interaction, which is identical to the force distribution for the head in the quiescent flow with the same movement. By replacing it by the linear combination of unit response, we get

$$\overrightarrow{\mathbf{f}_h} = -\mathbf{A}_{hh}^{-1} \cdot \mathbf{A}_{hf} \cdot \overrightarrow{\mathbf{f}_f} + v_T(0)\mathbf{f}_T^q + v_N(0)\mathbf{f}_N^q + \dot{\phi}(0)\mathbf{f}_K^q \tag{3.18}$$

To solve for the velocity and angular velocity in Equation (3.18), we substitute it into Equation (2.72) and (2.73):

$$v_T(0)\mathbf{F}_T^q + v_N(0)\mathbf{F}_N^q + \dot{\phi}(0)\mathbf{F}_K^q = \iint_{D_h} \left(\mathbf{A}_{hh}^{-1} \cdot \mathbf{A}_{hf} \cdot \overrightarrow{\mathbf{f}_f}\right) dD'_h + \mathbf{F}(0) \tag{3.19}$$

$$\dot{\phi}(0)\mathbf{M}_K^q = \iint_{D_h} x'_h \times \left(\mathbf{A}_{hh}^{-1} \cdot \mathbf{A}_{hf} \cdot \overrightarrow{\mathbf{f}_f}\right) dD'_h + \mathbf{x}(0) \times \mathbf{F}(0) + \int_0^1 N ds \tag{3.20}$$

With Equation (3.19) and (3.20), $\mathbf{v}(0)$ and $\dot{\phi}(0)$ can be solved and used in Equation (3.18)

to solve for the force distribution on the head.

3.4 Implicit Solver

As discussed before, only information necessary to solve for the flagellum part is force distribution, velocity and angular velocity of the head. If we manage to express these terms by the information from flagellum itself, we can couple these two parts and get rid of the iteration. In both Equation (3.19) and (3.20), we have the surface integral term on the right hand side. Because surface integral, dot product and cross product are all linear operator, we can group them into one operator, defined as

$$\iint_{D_h} \left(\mathbf{A}_{hh}^{-1} \cdot \mathbf{A}_{hf} \cdot \overrightarrow{\mathbf{f}_f} \right) dD_h' = \mathbf{B}_F \cdot \overrightarrow{\mathbf{f}_f} \tag{3.21}$$

$$\iint_{D_h} x_h' \times \left(\mathbf{A}_{hh}^{-1} \cdot \mathbf{A}_{hf} \cdot \overrightarrow{\mathbf{f}_f} \right) dD_h' = \mathbf{B}_M \cdot \overrightarrow{\mathbf{f}_f} \tag{3.22}$$

Equation (3.19) and (3.20) for the 2D beating can be written as

$$\begin{bmatrix} \mathbf{F}_T^q & \mathbf{F}_N^q \end{bmatrix} \cdot \begin{bmatrix} v_T(0) \\ v_N(0) \end{bmatrix} = \mathbf{B}_F \cdot \overrightarrow{\mathbf{f}_f} + \mathbf{F}(0) - \dot{\phi}(0)\mathbf{F}_K^q \tag{3.23}$$

$$\dot{\phi}(0)\mathbf{M}_K^q = \mathbf{B}_M \cdot \overrightarrow{\mathbf{f}_f} + \mathbf{x}(0) \times \mathbf{F}(0) + \int_0^1 N ds \tag{3.24}$$

We solve the angular velocity first, and then use it to solve for the velocity

$$\begin{bmatrix} v_T(0) \\ v_N(0) \end{bmatrix} = \begin{bmatrix} \mathbf{F}_T^q & \mathbf{F}_N^q \end{bmatrix}^{-1} \cdot \left(\mathbf{B}_F \cdot \overrightarrow{\mathbf{f}_f} + \mathbf{F}(0) - \frac{\mathbf{B}_M \cdot \overrightarrow{\mathbf{f}_f} + \mathbf{x}(0) \times \mathbf{F}(0) + \int_0^1 N ds}{\mathbf{M}_K^q} \mathbf{F}_K^q \right) \tag{3.25}$$

$$\dot{\phi}(0) = \frac{\mathbf{B}_M \cdot \overrightarrow{\mathbf{f}_f} + \mathbf{x}(0) \times \mathbf{F}(0) + \int_0^1 N ds}{\mathbf{M}_K^q} \tag{3.26}$$

In Equation (3.25) and (3.26), right hand side of the equation are linear operators fully given by the flagellum. We can further simplify it to be

$$v_T(0) = \mathbf{C}_1 \cdot \overrightarrow{\mathbf{F}}_{NT} \tag{3.27}$$

$$v_N(0) = \mathbf{C}_2 \cdot \overrightarrow{\mathbf{F}}_{NT} \tag{3.28}$$

$$\dot{\phi}(0) = \mathbf{C}_3 \cdot \overrightarrow{\mathbf{F}}_{NT} \tag{3.29}$$

With known $\mathbf{C}_1$, $\mathbf{C}_2$, $\mathbf{C}_3$, we move the corresponding terms in flagellum part on the right hand side to the left, and thus modified system as

$$\mathbf{A}'_{NT} \cdot \overrightarrow{\mathbf{F}}_{NT} = \mathbf{b}' \tag{3.30}$$

Then we have N and T along the flagellum by solving Equation (3.30) once only.

3.5 Time Marching

Based on Equation (2.68), the angular velocity of each flagellum segment can be calculated with Equation (3.31) after we calculate the force distribution in the system.

$$: \phi_t = \frac{1}{Sp^4}\left[N_{ss} + T\phi_{ss} + \left(1 + \frac{\xi_\perp}{\xi_\parallel}\right) T_s \phi_s - \frac{\xi_\perp}{\xi_\parallel} N \phi_s^2 + \xi_\perp \left(u_t^d \phi_s + \partial_s u_n^d\right)\right] \tag{3.31}$$

Velocity and angular velocity of head can be given by Equation (3.25) and (3.26). Dynein kinetics should be updated by Equation (2.71).

Chapter 4

Linear Stability Analysis

Before going to the simulation of nonlinear system with large deformations, we first apply the linear stability analysis with small perturbations. Compared to the later results for nonlinear simulation, by observing the dominating eigenvalue of the system we can successfully predict the existence and location of two bifurcations.

4.1 Assumption and Linearization

With very small perturbation of the flagellum, only very small force will be applied onto the head. The shape of head will only factor the solution slightly. To simplify the system, we assume the sperm cell is swimming with a spherical head in the quiescent flow with hydrodynamic interaction negligible. The non-local resistance force term $u_n^d = u_t^d = 0$, so the governing equations become

$$T_{ss} - N\phi_{ss} - (1 + \frac{\xi_{\parallel}}{\xi_{\perp}})N_s\phi_s - \frac{\xi_{\parallel}}{\xi_{\perp}}T\phi_s^2 = 0 \tag{4.1}$$

$$N_{ss} + T\phi_{ss} + (1 + \frac{\xi_{\perp}}{\xi_{\parallel}})T_s\phi_s - \frac{\xi_{\perp}}{\xi_{\parallel}}N\phi_s^2 = Sp^4\phi_t \tag{4.2}$$

$$\phi_{ss} + \mu_a f + N = 0 \tag{4.3}$$

$$f = \bar{n} - \zeta\tilde{n}\Delta_t - \frac{\mu}{\mu_a}\Delta \tag{4.4}$$

$$\partial_t n_\pm = \eta(1-n_\pm) - (1-\eta)n_\pm exp[\bar{f}(1\mp\zeta\Delta_t)] \tag{4.5}$$

The viscous force and torque acting on the spherical head in quiescent flow is known as $\mathbf{F}_{vis}^{head} = -6\pi\nu r\mathbf{v}(0)$ and $\mathbf{M}_{vis}^{head} = -8\pi\nu r^3\dot{\phi}(0)$, where r is the radius of the head. Then the nondimensionlized boundary conditions become

$$T(0) = \frac{3rSp^4}{4\xi_\perp}v^t(0) \tag{4.6}$$

$$N(0) = \frac{3rSp^4}{4\xi_\perp}\left(v^n(0) - r\dot{\phi}(0)\right) \tag{4.7}$$

$$rN(0) + \int_0^1 Nds = \frac{r^3Sp^4}{\xi_\perp}\dot{\phi}(0) \tag{4.8}$$

$$T(1) = 0 \tag{4.9}$$

$$N(1) = 0 \tag{4.10}$$

$$\phi_s(1) = 0 \tag{4.11}$$

4.2 Base State and Perturbation

Setting all time derivative terms to zero, we find the steady state at $\phi = const$. Here we choose this constant to be zero, so that the flagellum now aligned with x axis. From Equation (4.5), we got $n_{\pm 0} = n_0 = \frac{\pi_0}{\pi_0 + \varepsilon_0 e^{\bar{f}}}$. Combined with boundary condition, we find $f = 0$, $N = 0$, $T = 0$ at base state.

Then we add the perturbation to the system, $\phi = \delta\phi$ and $n_\pm = n_0 + \delta n_\pm$. Here we introduce $\delta n = \delta n_+ = -\delta n_-$. Similarly, $f = \delta f, T = \delta T, N = \delta N$. Also, we consider $\bar{f}\zeta\phi_t \ll 1$.

Substituting into the governing equations and linearizing the system, we get

$$\delta T_{ss} = 0 \tag{4.12}$$

$$\delta N_{ss} = Sp^4 \delta \phi_t \tag{4.13}$$

$$\delta \phi_{ss} + \mu_a \delta f + \delta N = 0 \tag{4.14}$$

$$\delta f = 2\delta n - 2\zeta n_0 \delta \Delta_t - \frac{\mu}{\mu_a} \delta \Delta \tag{4.15}$$

$$\delta n_t = (1-\eta) e^{\bar{f}} n_0 \bar{f} \zeta \delta \Delta_t - \frac{\eta}{n_0} \delta n \tag{4.16}$$

Using the fact that $\partial_s \Delta = \partial_s \phi$, we apply ∂_s on Equation (4.15) and (4.16)

$$\delta f_s = 2\delta n_s - 2\zeta n_0 \delta \phi_{ts} - \frac{\mu}{\mu_a} \delta \phi_s \tag{4.17}$$

$$\delta n_{ts} = (1-\eta) e^{\bar{f}} n_0 \bar{f} \zeta \delta \phi_{ts} - \frac{\eta}{n_0} \delta n_s \tag{4.18}$$

4.3 Normal Mode

Assume all perturbation has the form $\delta A = \tilde{A} e^{\sigma t} e^{iks}$, where A can be T, N, ϕ, f, n. Substitute to Equation (4.12), (4.13), (4.14), (4.17), (4.18), we get

$$-k^2 \tilde{T} = 0 \tag{4.19}$$

$$-k^2 \tilde{N} = Sp^4 \sigma \tilde{\phi} \tag{4.20}$$

$$-k^2 \tilde{\phi} + \mu_a \tilde{f} + \tilde{N} = 0 \tag{4.21}$$

$$\tilde{f} = 2\tilde{n} - 2\zeta n_0 \sigma \tilde{\phi} - \frac{\mu}{\mu_a} \tilde{\phi} \tag{4.22}$$

$$\sigma\tilde{n} = (1-\eta)e^{\bar{f}}n_0\bar{f}\zeta\sigma\tilde{\phi} - \frac{\eta}{n_0}\tilde{n} \tag{4.23}$$

For Equation (4.19) to be satisfied without having a trivial solution, $\tilde{T} = 0$. We now use $\tilde{\phi}$ as the only variable. From eqn. (4.20), (4.22), (4.23)

$$\tilde{N} = -\frac{Sp^4\sigma}{k^2}\tilde{\phi} \tag{4.24}$$

$$\tilde{n} = \chi'\tilde{\phi} \tag{4.25}$$

$$\tilde{f} = \chi\tilde{\phi} \tag{4.26}$$

Where, $\chi' = n_0(1-n_0)\bar{f}\zeta\frac{\sigma\eta}{\sigma n_0+\eta}$, and $\chi = 2\chi' - 2\zeta n_0\sigma - \frac{\mu}{\mu_a}$. Substitute Equation(4.24), (4.26) into (4.21) and cancel $\tilde{\phi}$, we get

$$k^4 - \mu_a\chi k^2 + Sp^4\sigma = 0 \tag{4.27}$$

which is quartic equation for k, with four roots, so we can write $\delta A = \sum_{j=1}^{4}\tilde{A}_j e^{ik_j s}e^{\sigma t}$, where A can be T, N, ϕ, f, n.

4.4 Boundary Conditions

From the slender body theory, we have $N_s + T\phi_s = Sp^4 v_N$. Since $T = 0$ from eqn.(4.19), we have $v_N = Sp^{-4}N_s$. Then eqn.(4.7) becomes

$$N(0) = \frac{3rSp^4}{4\xi_{\parallel}}\left(Sp^{-4}N_s(0) - r\dot{\phi}(0)\right) \tag{4.28}$$

Substitute normal modes into eqn. (4.28), (4.8), (4.10), (4.11), we get

$$\sum_{j=1}^{4}\left[\left(\frac{3ir}{4\xi_{\perp}}k_j^{-1} + \frac{3r^2}{4\xi_{\perp}} - k_j^{-2}\right)\Phi_j\right] = 0 \tag{4.29}$$

$$\sum_{j=1}^{4}\left\{\left[ik_j^{-3}\left(1-e^{ik_j}\right)+rk_j^{-2}+\frac{r^3}{\xi_\perp}\right]\Phi_j\right\}=0 \tag{4.30}$$

$$\sum_{j=1}^{4}\left(ik_j e^{ik_j}\Phi_j\right)=0 \tag{4.31}$$

$$\sum_{j=1}^{4}\left(k_j^{-2}e^{ik_j}\Phi_j\right)=0 \tag{4.32}$$

4.5 Bifurcations

4.5.1 Methodology

Here we re-write Equation (4.29), (4.30), (4.31), (4.32) as

$$\mathbf{G}\cdot\Phi=0 \tag{4.33}$$

Where $\mathbf{G}$ is the coefficients we get that include k_j as the root of Equation (4.27), and $\Phi=[\Phi_1,\Phi_2,\Phi_3,\Phi_4]^T$. The characteristic equation for this system is written as

$$det(\mathbf{G})=0 \tag{4.34}$$

while its roots are defined as the eigenvalues of the system that can be used to predict the stability condition for this problem.

The characteristic equation has been solved numerically. With a specific Sp and μ_a, we search σ in the complex plane and plot the value of determinant of $\mathbf{G}$, so that we can approximately locate the roots by inspection. Then we use the function *Findroot* in software *Mathematica*, and use the approximate guess as the initial guess to determine the more specific location of roots.

4.5.2 Dominant Eigenvalue

It is σ in the expression $\delta A = \sum_{j=1}^{4} \tilde{A}_j e^{ik_j s} e^{\sigma t}$ that governs the development for the mode over the time. We define the eigenvalue with the largest real part as the dominant eigenvalue.

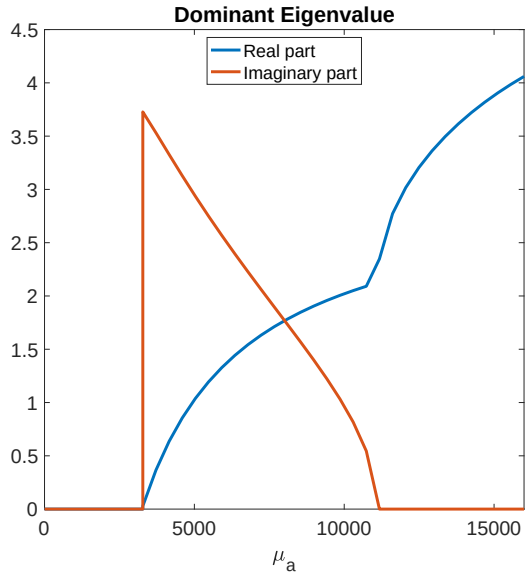

Figure 4.1: Real and imaginary part of dominant eigenvalue with $Sp = 8$.

With $Sp = 8$, Figure 4.1 marks the real and imaginary part of dominant eigenvalue as a function of μ_a. When the activity is low, the dominant eigenvalue stays at the origin point in the complex plane until a pair of eigenvalues reach the imaginary axis. Then it gradually moves toward the real axis with increasing activity and further moves toward the right. It finally reaches to the real axis and the slope of real part suddenly increases with μ_a.

4.5.3 Marginal Stability

As shown in Figure 4.1, there are two important bifurcations in the system. The first bifurcation marks the marginal stability of the system. If all eigenvalues of the system have a negative real part, the perturbation will decay to non-perturbed state eventually. So the sign of real part of dominant eigenvalue decides whether the system is steady or will amplify the perturbation

and thus create the spontaneous oscillation. The bifurcation between stable and unstable regimes happens when the dominant eigenvalue sits right on the imaginary axis. Searching in the parameter plane of Sp and μ_a, we can mark the marginal stability boundary line as shown in Figure 4.2.

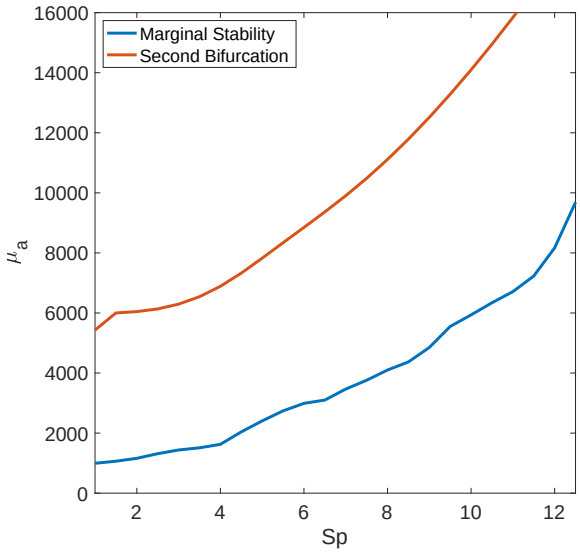

Figure 4.2: Marginal stability line and second bifurcation in parameter plane based on linear stability analysis.

4.5.4 Second Bifurcation

Within the unstable region above the marginal stability line, there has been at least one pair of conjugate eigenvalues reach the right half of the parameter plane. While the positive real part of the eigenvalues amplifies the mode, imaginary part of the eigenvalue offers the oscillation. For a eigenvalue sitting on the real axis, it no longer produces the oscillation to the system. It can be interesting when the imaginary part of the dominant eigenvalue goes to zero as observed in Figure 4.1. At this point, the beating is no longer generated by the dominant eigenvalue but by the rest of the modes. We call this line the second bifurcation, and also mark it in the parameter plane as in Figure 4.2.

Chapter 5

Results

In the previous chapters, we have proposed the governing equations and boundary conditions. Following the partially implicit numerical methods that factored the long range interaction between head and flagellum, we successfully simulate the swimming of sperm cell with different parameters. In this chapter, we observe the simulation results from different aspects. We first start with the beating shape and swimming direction, finding that there exist two different beating patterns characterized by different shapes, while both swim forward with the curvature propagating from base to tip. Then we calculate the velocity and vorticity domain, and the average velocity for both close and far region within the co-moving frame. Several transitions have been observed with different methods, to separate the parameter plane into two regions. To better understand the swimming, we have also defined several swimming characteristics, with the results showing that some of them are not monotonically controlled by the parameters in specific regions. In the end of this chapter, we look at the energetics of the system, studying the dissipation and efficiency of this biological system.

5.1 Beating and Swimming

For the cases that the sperm cell has ability to amplify the initial perturbation and exhibit spontaneous beating, the swimming movement will reach a steady periodic stage after several beating cycles. The swimming shape can be depicted by the stroboscopic view in Figure 5.1, where (a) and (b) show two different beating patterns that can be observed in the parameter plane. The sperm cell with relatively smaller activity beat as shown in Figure 5.1 (a) where a spindle shape is enveloped by the beating. When we further increase the activity up to point, we can observe the beating shape like in Figure 5.1 (b). The first pattern has larger head rotation and smoother curvature distribution, while the rotation of head in the second pattern in more restricted, with large curvature concentrated at the section near to the middle and the end.

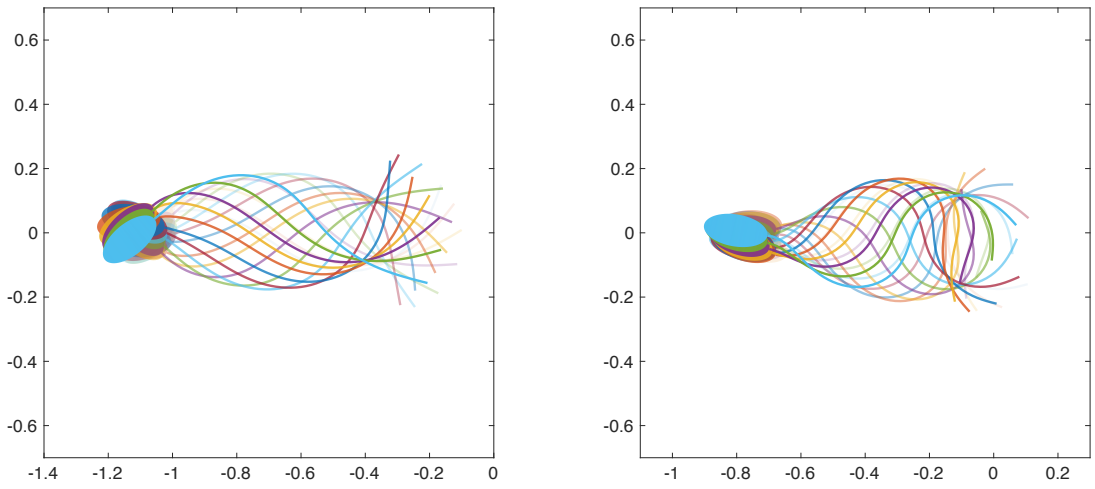

(a) (b)

Figure 5.1: Stroboscopic view of two typical beating pattern. Simulation parameters: (a) $Sp = 4$, $\mu_a = 5820$; (b) $Sp = 4$, $\mu_a = 10910$.

In the previous study, flagellum clamped on the wall is noticed to have a second bifurcation that divide the two beating modes with different curvature wave propagation direction [32]. In this study where the sperm can freely swim in the viscous environment, the curvature is always propagating from the base end to the distal end. With such a wave, the sperm cell in all the cases

swims in the forward direction. Further, we also observed the transition by its beating shape instead of the wave propagation direction. In the later section, we will discuss this bifurcation in more detail.

5.2 Flow Fields

Looking more closely at one parameter combination, we use boundary integral method to evaluate the velocity and vorticity in the flow domain.

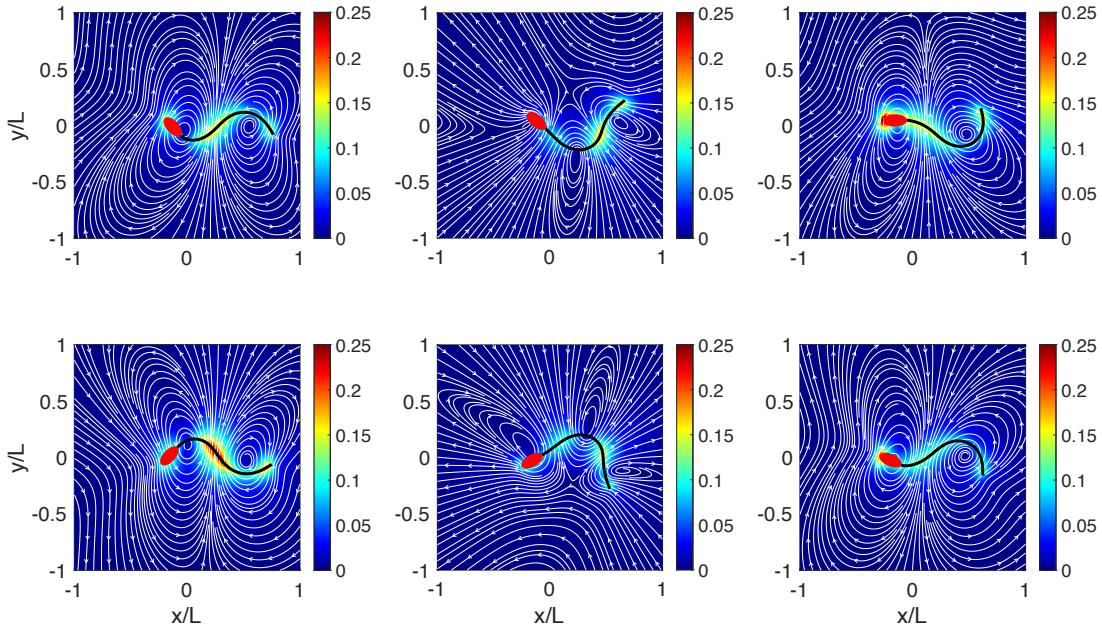

Figure 5.2: Snapshots of streamline and velocity magnitude in flow domain. Simulation parameters: $Sp = 5$, $\mu_a = 8000$.

The snapshots of velocity magnitude and streamline over one beating period is illustrated as Figure 5.2. For the side to side beating of sperm cell, two local maximum velocity magnitude region are generated in one cycle. The large velocity region is first generated in front of the head and gradually covers and climb over the head surface down to the flagellum. Once it reaches flagellum at the connection point, it starts to propagate along the flagellum from base to tip. After

the region gets to the distal end, it starts to accumulate at the tip, and vanish at last. Streamlines in the figure indicates the existence of vortices in the domain, where we can see vortex with different direction show up side by side, creating the local maximum velocity region at the boundary of two vortices.

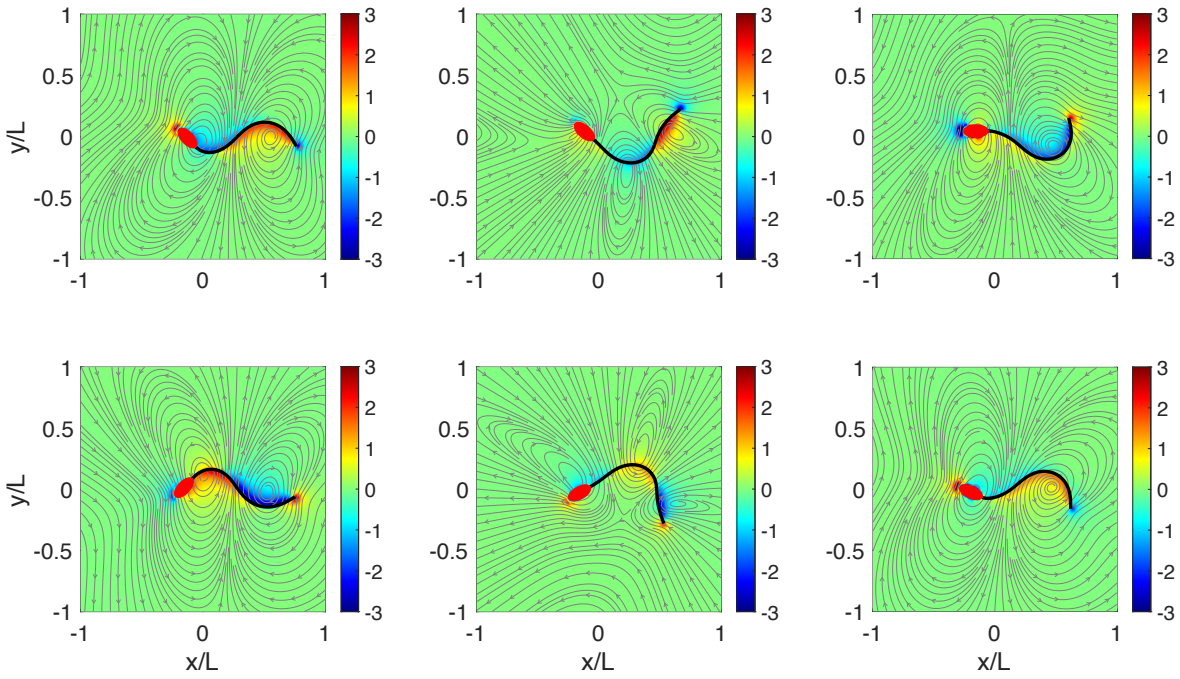

Figure 5.3: Snapshots of streamline and vorticity in flow domain. Simulation parameters: $Sp = 5$, $\mu_a = 8000$.

The distribution of vorticity in the flow domain is shown as in Figure 5.3. As we can observed before from the streamline, positive and negative vortices are generated alternately in front of the head, propagate along the flagellum, accumulate and vanish at the distal end. Different from the velocity, local maximum vorticity magnitude stand right on the center of the vortices, and tend to show up at the concave side of the bending flagellum.

Figure 5.4 shows the normalized average velocity in the near region and in a larger domain. Since the sperm cell is swimming forward, to evaluate the mean value of the velocity after the sperm reaching its steady periodic beating, sperm cell and its domain is observed in

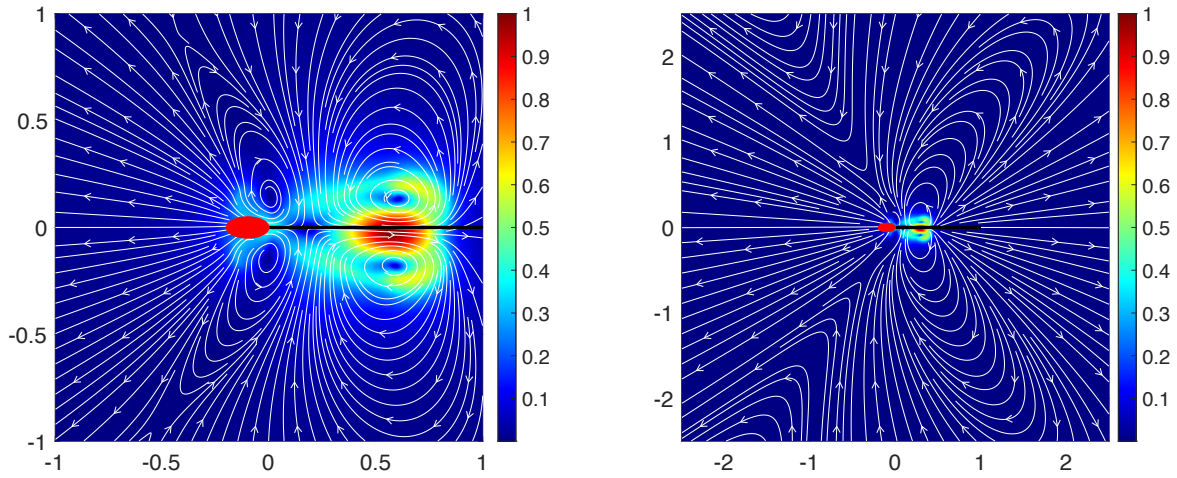

Figure 5.4: Average flow field in co-moving frame. Simulation parameters: $Sp = 5$, $\mu_a = 8000$.

the co-moving frame. In Figure 5.4 (a), the average flow near the sperm cell shows two pairs of vortices symmetric about the flagellum. The relatively smaller pair contact with other side at the connecting point, while the larger pair is much more dominant, creating a large average velocity region near the middle section of the flagellum. Regarding the far domain, Figure 5.4 (b) indicates that the flagellum mostly works as a force dipole in the domain, creating the flow starting from the head and distal end of the flagellum. There also exists a large pair of vortices at the middle section.

5.3 Transitions

In the chapter on linear stability analysis, we predicted the existence of the marginal stability and the second bifurcation. Here by observing the performance of the simulation results of the nonlinear system, we mark several transition lines in the parameter plane.

The pink line in Figure 5.5 represents the first bifurcation as marginal stability line of the system. Below the line is the stable region, where the activity is not enough to trigger the

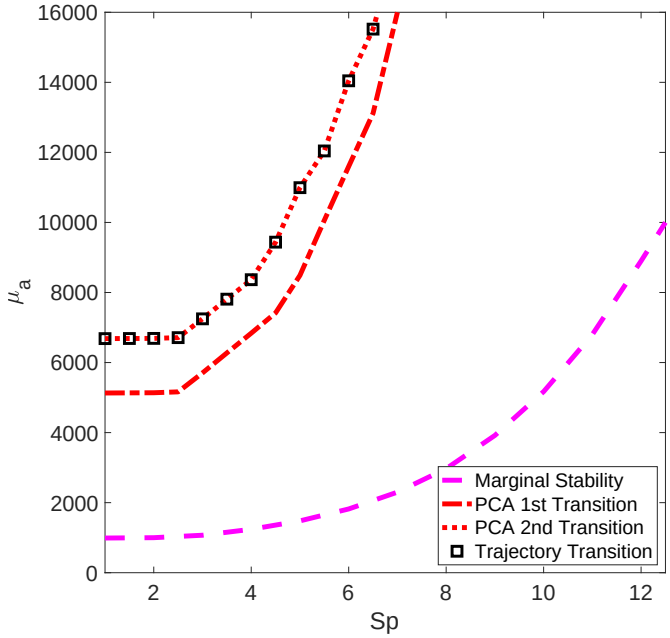

Figure 5.5: Transitions in parameter plane.

oscillation starting from the perturbation. The region above the marginal stability line is the unstable region, where we can observe the spontaneous beating and swimming.

We apply the Principle Component Analysis (PCA) onto the curvature of the flagellum as a function of time. The linear combination of first two modes can correctly represent over 90% information of the beating. By observing the shape of the first two dominant modes, we find three patterns in the parameter plane as shown in Figure 5.6. The pattern in (a) shows up starting from the marginal stability line, with relatively smaller activity. The pattern in (b) only exists within a narrow band in the parameter plane, followed with the third pattern in (c). The transition between these three patterns is marked by the two red lines as shown in Figure 5.5.

Figure 5.7 shows the corresponding head trajectory of the two beating patterns observed in Figure 5.1. Both patterns swim forward, which is leftward in the current frame. From the top of the trajectory to the bottom, (a) with relatively smaller activity goes backward and then forward, while the pattern shown in (b) goes forward and then backward. There is a clear transition

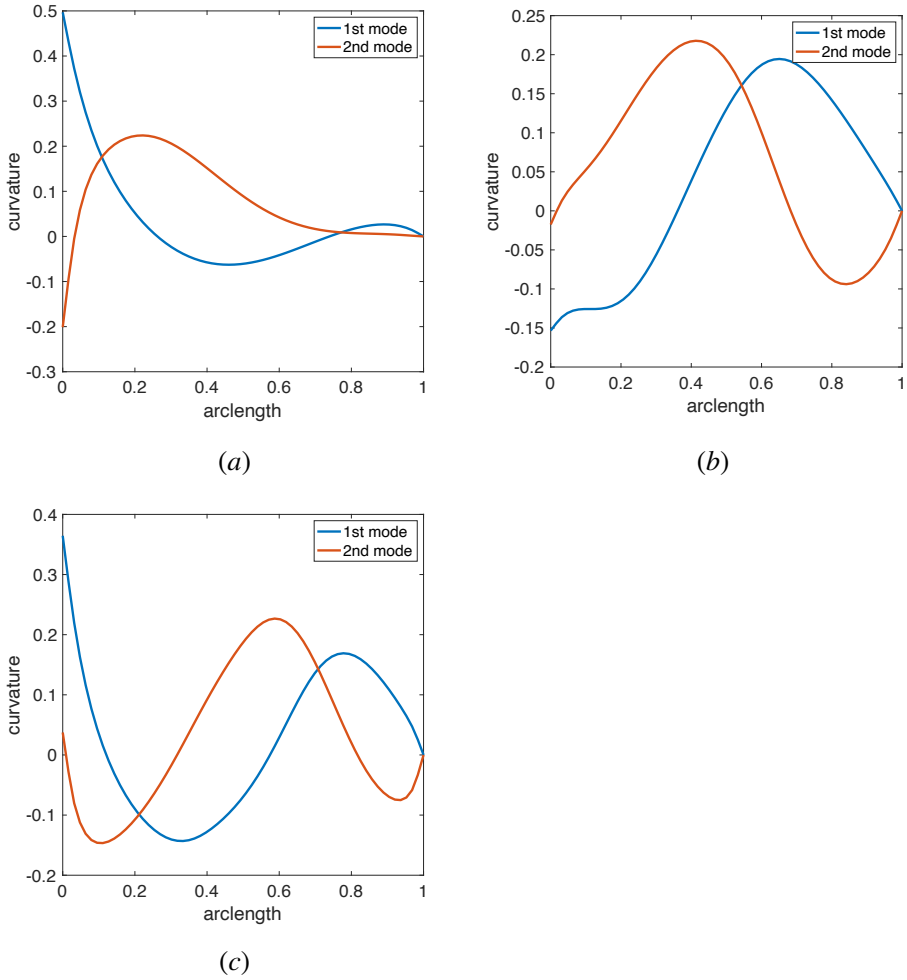

Figure 5.6: First two mode of Principle Component Analysis of curvature along flagellum. Simulation parameters: (a) $Sp = 4$, $\mu_a = 1749$; (b) $Sp = 4$, $\mu_a = 6839$; (c) $Sp = 4$, $\mu_a = 11928$.

between these two patterns, and happens at the same time as the second PCA transition as shown in Figure 5.5.

These transitions divide the parameter plane into several regions. The region below the marginal stability line is called the stable region. For the unstable region above the marginal stability line, we call the part under the first PCA transition as the lower region, and that above the second PCA transition as the upper region.

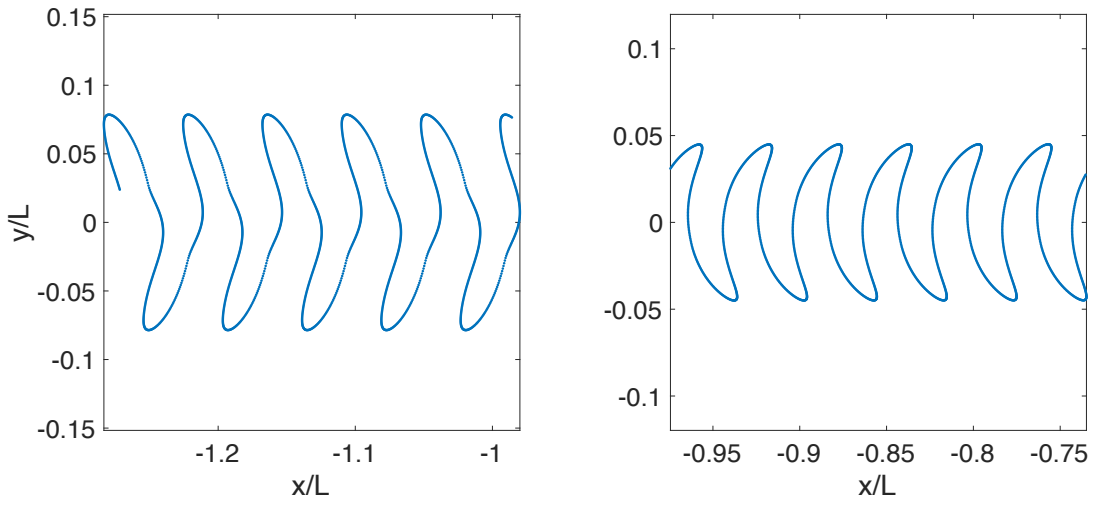

(*a*) (*b*)

Figure 5.7: Two patterns of head trajectory. Simulation parameters: (a) $Sp = 4$, $\mu_a = 5312$; (b) $Sp = 4$, $\mu_a = 9892$.

5.4 Swimming Characteristics

The beating of the flagellum manages to push the head forward by propagating the curvature wave from base to tip. The goal of the sperm cell movement is to transport the genetic information carrier DNA to the egg. Even though the trajectories show that the head oscillates side to side during swimming, forward marching is the ultimate purpose. In this section we study the movement of head by defining several swimming characteristics.

The rotation and side to side oscillation are typical motion that steer the swimming direction of sperm cell. For the symmetric beating in our simulation results, the total displacement of the head is a straight line pointing in the forward direction, which makes oscillations nothing but a waste of energy. We evaluate the beating amplitude as the distance between upper and lower boundary of the trajectory, with Figure 5.8 showing its dependence on Sp and μ_a. It is non monotonically controlled by the parameters in the lower region, where we can find the maximum amplitude zone with larger Sp and μ_a near the first PCA transition. In the upper region, the

amplitude increases with smaller Sp and larger μ_a.

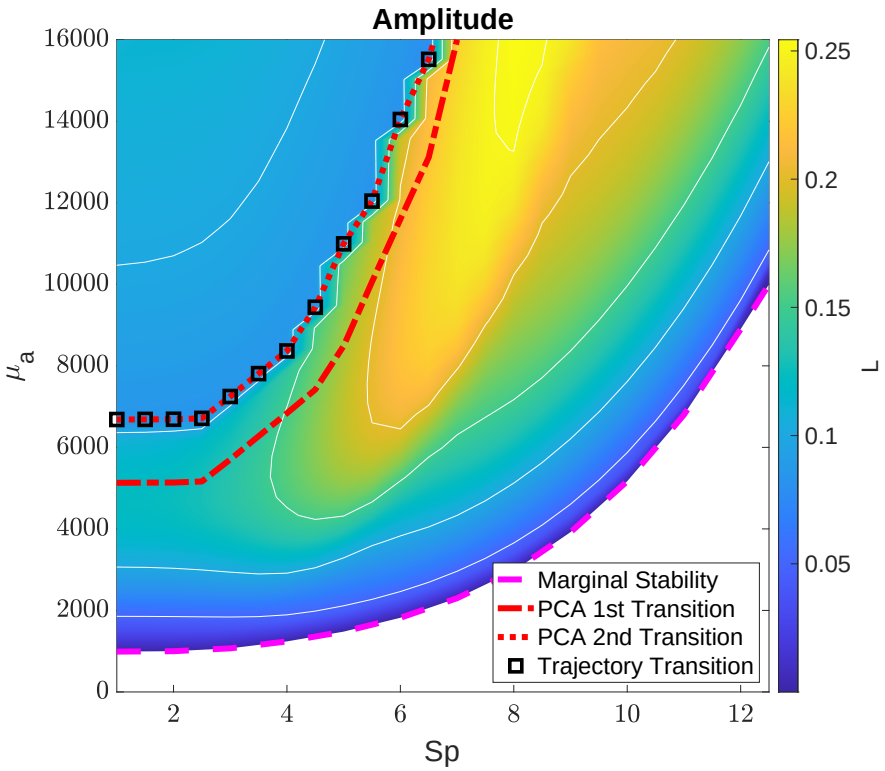

Figure 5.8: Side-to-side beating amplitude.

The head and flagellum have their own frequency distribution in the frequency domain. However we find their dominant frequency to be identical, which is evaluated here. Figure 5.9 shows the contour of the dominant frequency in the parameter plane. With the least activity right above the marginal stability line, we find the largest beating frequency. In both the upper and lower regions the frequency is mostly dominated by the activity, while the frequency decrease with larger activity in the lower region, and slightly decreases with larger activity in the upper region.

Since the forward marching is the ultimate purpose of sperm cell, the velocity in the forward direction is very important for a given active beating. The forward velocity is defined as the average velocity in the forward direction over a period. In the contour shown in Figure

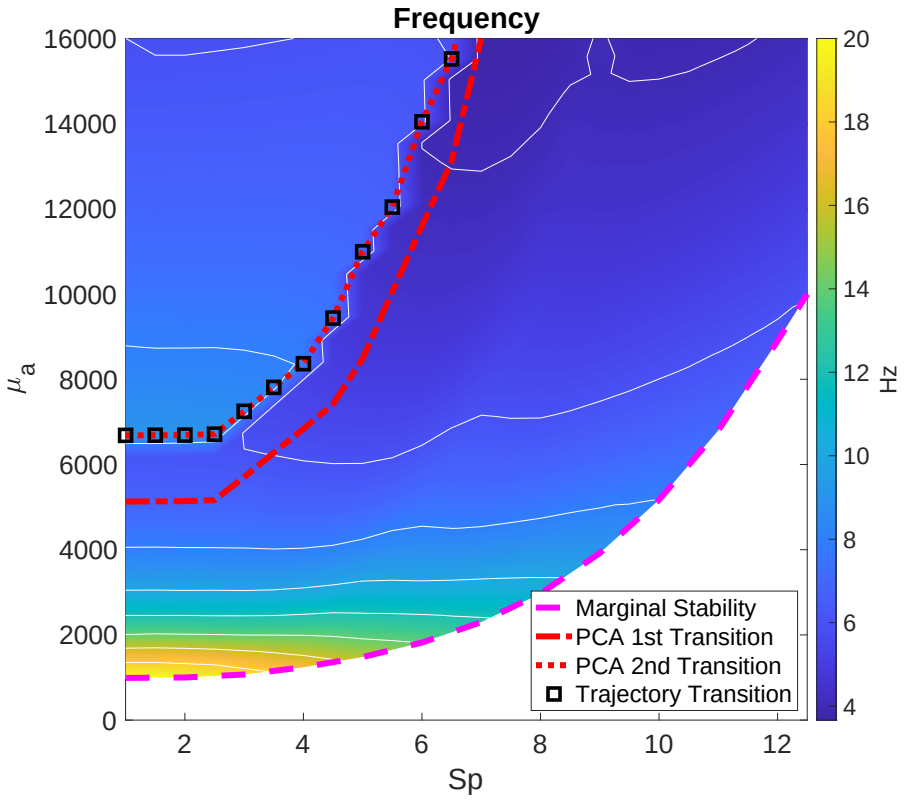

Figure 5.9: Dominant frequency of the sperm cell.

5.10, we can see the velocity is non monotonic in the lower region. With activity right above the marginal stability line, even though the sperm beats at a large frequency, the beating is almost local. When we further increase the activity, the velocity suddenly increases and reaches its maximum region. The maximum region is located near the first PCA transition similar to the amplitude, but closer to the small Sp. For one parameter combination, it is hard for a trajectory to have both large amplitude and forward displacement with fixed active input, which makes it reasonable to observe the maximum zone of magnitude and velocity locate differently. In the upper region the velocity is mostly dominated by the activity, and monotonically decreases with larger activity.

We are interested in the energy efficiency of this biological system. We write the energy

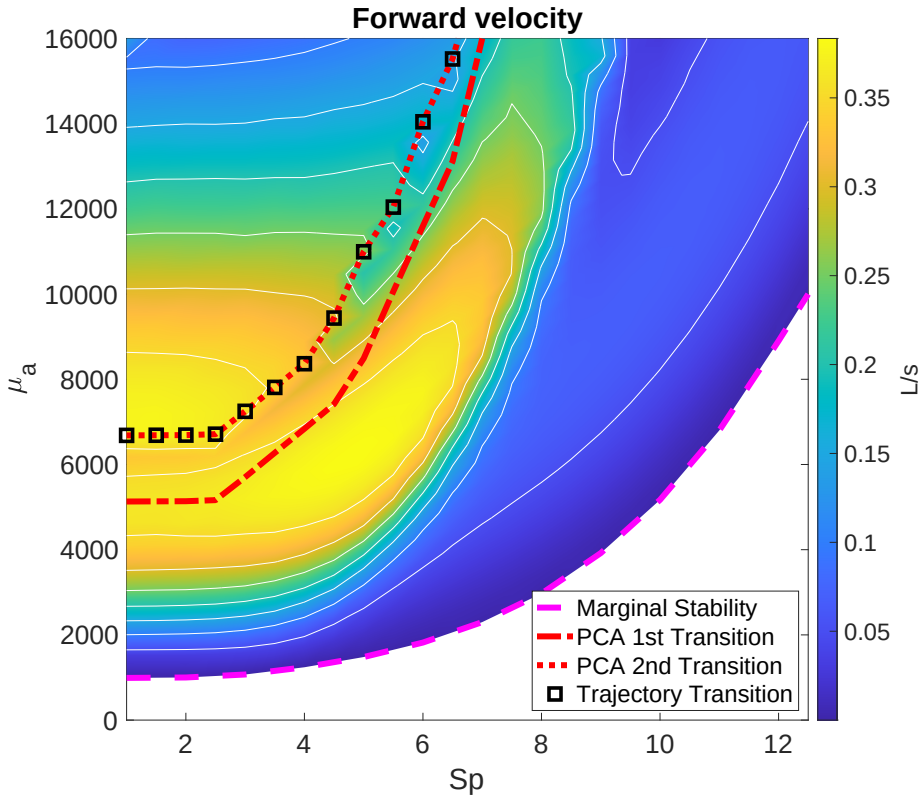

Figure 5.10: Forward swimming velocity of sperm cell.

balance equation of the system as

$$\frac{dE}{dt} + P_d = P_a \tag{5.1}$$

where $\frac{dE}{dt}$ is the change rate of the total elastic energy stored in the flagellum, P_d is the total viscous dissipation of the system, and P_a is the total active input given by dynein motors.

After the beating reaching its steady stage with same shape of the flagellum after a cycle of beating, there will be no difference of the elastic energy stored in flagellum, so that we can write

$$\int_t^{t+T} P_a dt = W_d \tag{5.2}$$

where $W_d = \int_t^{t+T} P_d dt$.

If we define the forward marching as the purpose, the minimum possible dissipation

would be for the case of one inactive and undeformed sperm cell moving the same distance over a period with the same velocity, written as $W_{min} = F_d \cdot l$. The viscous force $F_d = Cv_{avg}$ is linear in the velocity based on the linearity of Stokes flow. The displacement over a period in the active case can be given by velocity and frequency $l = v_{avg}/f_{freq}$. The efficiency $\varepsilon = \frac{W_{min}}{W_d}$ can then be expressed as

$$\varepsilon = \frac{Cv_{avg}^2}{f_{freq} \cdot \int_t^{t+T} \int_0^1 f \Delta_t ds dt} \tag{5.3}$$

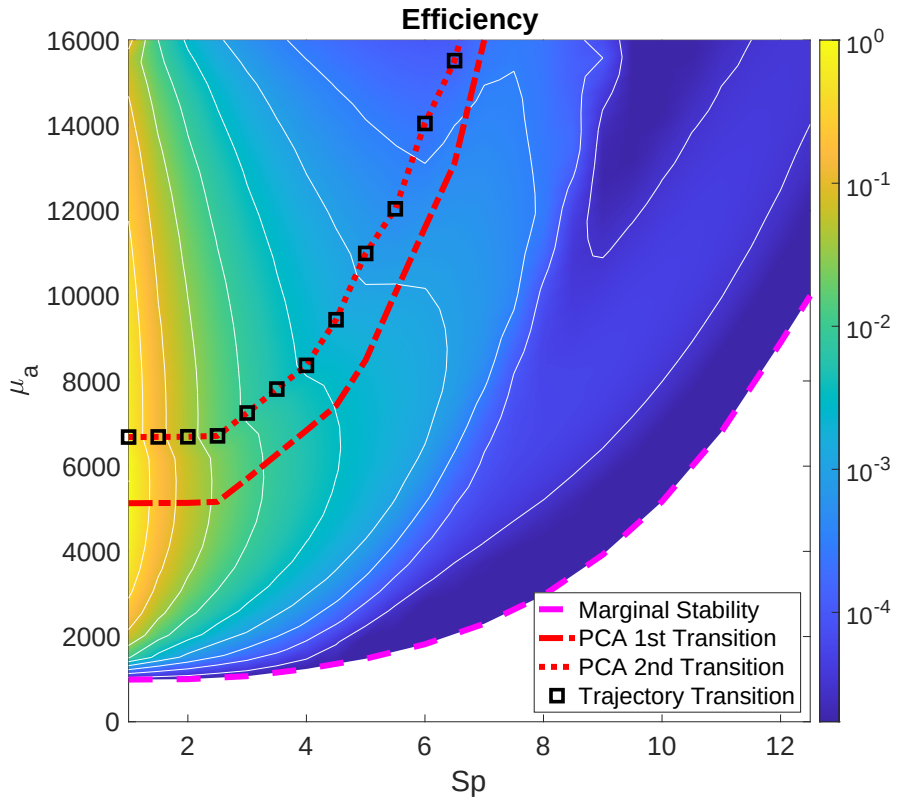

Figure 5.11: Normalized efficiency of the system.

Figure 5.11 illustrates the contour of normalized efficiency. Logarithm color bar indicates that the efficiency of the system is mostly dominated by the rigidity of the system. For a specific Sp, best efficiency always show up at the place where maximum velocity exists.

Chapter 6

Conclusions

In this thesis, I numerically solved for the motion of a sperm cell freely swimming with the spontaneous beating governed by a sliding control model. Slender body theory and boundary integral method are used here to include not only the local resistance but also long range hydrodynamic interaction between head and flagellum and between different parts of flagellum. An implicit numerical solver coupling the hydrodynamic interaction was proposed, which can solve the system dozens to thousands of time faster then the explicit solver.

Under the assumption of small shape perturbations, we applied a linear stability analysis to the system. A Hopf bifurcation can be marked where the unstable modes start to drive the spontaneous beating. By tracking the dominant eigenvalue of the system, we can also predict the existence of the second transition where the dominant mode no longer provides oscillation to the system.

The simulation results of the nonlinear system is found to have similar pattern as predicted by linear stability analysis. While the Hopf bifurcation is defined by the motility, the second transition in parameter plane of sperm number and activity can be marked by different patterns of head trajectories, PCA modes and the shape enveloped by the beating flagellum. Through whole parameter domain, sperm cells are observed to keep swimming forward. Unlike the clamped

flagellum [32], the curvature wave with freely swimming condition is always propagating from base to tip.

As for the motility of sperm cell, flow fields show that both velocity and vorticity have their local maxima first appear in front of the head, propagate along the flagellum, accumulate and vanish at the distal end. Swimming characteristics are showen to be smooth in both the upper and lower regions and not always monotonically controlled by the rigidity or activity. The frequency of the head oscillation is mostly controlled by activity, and the efficiency of the biological system is mostly decided by the sperm number. Head beating amplitude and sperm forward swimming velocity are both found to be non monotonic in the lower region, with their maximum region right under the first PCA transition.

Bibliography

[1] E. A. Gaffney, H. Gadêlha, DJ Smith, JR Blake, and Jackson C Kirkman-Brown. Mammalian sperm motility: observation and theory. *Annual Review of Fluid Mechanics*, 43:501–528, 2011.

[2] Don W Fawcett. The mammalian spermatozoon. *Developmental Biology*, 44(2):394–436, 1975.

[3] Gary E Olson and Richard W Linck. Observations of the structural components of flagellar axonemes and central pair microtubules from rat sperm. *Journal of Ultrastructure Research*, 61(1):21–43, 1977.

[4] Alan C Menge and Robert P Edwards. Mucosal immunity of the reproductive tract and infertility. *Immunology of Reproduction*, 54:51–55, 1993.

[5] Susan S Suarez and AA Pacey. Sperm transport in the female reproductive tract. *Human Reproduction Update*, 12(1):23–37, 2006.

[6] Anthony Hirsh. Male subfertility. *Bmj*, 327(7416):669–672, 2003.

[7] World Health Organization. Prevention and management of infertility: Progress. *World Health Organization, Geneva, Switzerland*, page 15, 1990.

[8] Stephanie T Page, John K Amory, and William J Bremner. Advances in male contraception. *Endocrine Reviews*, 29(4):465–493, 2008.

[9] Yuki Hirano, Hiroaki Shibahara, Hiromi Obara, Tatsuya Suzuki, Satoru Takamizawa, Chieko Yamaguchi, Hiromichi Tsunoda, and Ikuo Sato. Andrology: Relationships between sperm motility characteristics assessed by the computer-aided sperm analysis (casa) and fertilization rates in vitro. *Journal of Assisted Reproduction and Genetics*, 18(4):215–220, 2001.

[10] P Morales, JW Overstreet, and DF Katz. Changes in human sperm motion during capacitation in vitro. *Reproduction*, 83(1):119–128, 1988.

[11] Chiara Boschetto, Clelia Gasparini, and Andrea Pilastro. Sperm number and velocity affect sperm competition success in the guppy (poecilia reticulata). *Behavioral Ecology and Sociobiology*, 65(4):813–821, 2011.

[12] Don R Levitan. Sperm velocity and longevity trade off each other and influence fertilization in the sea urchin lytechinus variegatus. *Proceedings of the Royal Society of London. Series B: Biological Sciences*, 267(1443):531–534, 2000.

[13] Gary Burness, Stephen J Casselman, Albrecht I Schulte-Hostedde, Christopher D Moyes, and Robert Montgomerie. Sperm swimming speed and energetics vary with sperm competition risk in bluegill (lepomis macrochirus). *Behavioral Ecology and Sociobiology*, 56(1):65–70, 2004.

[14] TR Birkhead, JG Martinez, T Burke, and DP Froman. Sperm mobility determines the outcome of sperm competition in the domestic fowl. *Proceedings of the Royal Society of London. Series B: Biological Sciences*, 266(1430):1759–1764, 1999.

[15] Aurelio F Malo, J Julián Garde, Ana J Soler, Andrés J García, Montserrat Gomendio, and Eduardo RS Roldan. Male fertility in natural populations of red deer is determined by sperm velocity and the proportion of normal spermatozoa. *Biology of Reproduction*, 72(4):822–829, 2005.

[16] HARRY DM MOORE and MEHDI A AKHONDI. Fertilizing capacity of rat spermatozoa is correlated with decline in straight-line velocity measured by continuous computer-aided sperm analysis: epididymal rat spermatozoa from the proximal cauda have a greater fertilizing capacity in vitro than those from the distal cauda or vas deferens. *Journal of Andrology*, 17(1):50–60, 1996.

[17] Jun Liu, Clement Leung, Zhe Lu, and Yu Sun. Quantitative analysis of locomotive behavior of human sperm head and tail. *IEEE Transactions on Biomedical Engineering*, 60(2):390–396, 2012.

[18] Bruce Alberts, Dennis Bray, Karen Hopkin, Alexander D Johnson, Julian Lewis, Martin Raff, Keith Roberts, and Peter Walter. *Essential cell biology*. Garland Science, 2015.

[19] Ingmar H Riedel-Kruse, Andreas Hilfinger, Jonathon Howard, and Frank Jülicher. How molecular motors shape the flagellar beat. *HFSP Journal*, 1(3):192–208, 2007.

[20] James Gray and GJ Hancock. The propulsion of sea-urchin spermatozoa. *Journal of Experimental Biology*, 32(4):802–814, 1955.

[21] Benjamin M Friedrich, Ingmar H Riedel-Kruse, Jonathon Howard, and Frank Jülicher. High-precision tracking of sperm swimming fine structure provides strong test of resistive force theory. *Journal of Experimental Biology*, 213(8):1226–1234, 2010.

[22] Johannes Martinus Burgers. On the motion of small particles of elongated form suspended in a viscous liquid. *Kon. Ned. Akad. Wet. Verhand.(Eerste Sectie)*, 16:113–184, 1938.

[23] GI Taylor. Motion of axisymmetric bodies in viscous fluids. *Problems of Hydrodynamics and Continuum Mechanics*, pages 718–724, 1969.

[24] Constantine Pozrikidis. *A practical guide to boundary element methods with the software library BEMLIB*. CRC Press, 2002.

[25] PV Bayly and SK Dutcher. Steady dynein forces induce flutter instability and propagating waves in mathematical models of flagella. *Journal of The Royal Society Interface*, 13(123):20160523, 2016.

[26] Tianchen Hu and Philip V Bayly. Finite element models of flagella with sliding radial spokes and interdoublet links exhibit propagating waves under steady dynein loading. *Cytoskeleton*, 75(5):185–200, 2018.

[27] Charles J Brokaw. Bend propagation along flagella. *Nature*, 209(5019):161–163, 1966.

[28] Michael Hines and JJ Blum. Bend propagation in flagella. i. derivation of equations of motion and their simulation. *Biophysical Journal*, 23(1):41–57, 1978.

[29] Charles B Lindemann. A" geometric clutch" hypothesis to explain oscillations of the axoneme of cilia and flagella. *Journal of Theoretical Biology*, 168(2):175–189, 1994.

[30] R Dillon, L Fauci, and Charlotte Omoto. Mathematical modeling of axoneme mechanics and fluid dynamics in ciliary and sperm motility. *Dynamics of Continuous Discrete and Impulsive Systems Series A*, 10:745–758, 2003.

[31] David Oriola, Hermes Gadêlha, and Jaume Casademunt. Nonlinear amplitude dynamics in flagellar beating. *Royal Society Open Science*, 4(3):160698, 2017.

[32] Brato Chakrabarti and David Saintillan. Spontaneous oscillations, beating patterns, and hydrodynamics of active microfilaments. *Physical Review Fluids*, 4(4):043102, 2019.

[33] JM Cummins and PF Woodall. On mammalian sperm dimensions. *Reproduction*, 75(1):153–175, 1985.

[34] Matthew JG Gage. Mammalian sperm morphometry. *Proceedings of the Royal Society of London. Series B: Biological Sciences*, 265(1391):97–103, 1998.